ORIGINAL

Evolution of fault patterns within a zone of pre-existing pervasive anisotropy during two successive phases of extensions: an experimental study

N. Ghosh[1] · K. Hatui[1] · A. Chattopadhyay[1]

Abstract

The aim of the present work is to study the influence of preexisting pervasive strength anisotropy on the development of faults during two phases of extensions. Two different series of experiments are performed by deforming rectangular three-layered models either by orthogonal extension followed by oblique extension (series 1) or by oblique extension followed by orthogonal extension (series 2). The model represents a rectangular zone of rifting. The final fault architecture after two successive phases of extension is primarily controlled by the orientation of the pervasive strength anisotropy. The mode of far-field stress (orthogonal or oblique) plays a role in fault initiation during both the phases of extension. The growth of the faults which are orthogonal or oriented more obliquely ($\beta = 45°/60°$) with respect to the rift normal is controlled by the direction of extension. However, the less oblique faults ($\beta = 15°$) develop as strike-slip faults irrespective of the direction of extension. The phase 1 faults reactivate during the phase 2 extension only when they are parallel to the preexisting pervasive anisotropy. New faults parallel to the rift axis form only if the phase 2 extension is orthogonal (series 2). It is found to happen irrespective of the orientation of the strength anisotropy and of the 1st phase faults. Those faults act as linking faults for the highly oblique ($\beta = 45°/60°$) phase 1 faults. New faults are formed following the anisotropy during both orthogonal and oblique phase 2 extension only if the anisotropy is oriented at low angle ($\beta = 15°$) with the rift normal. The different fault patterns developed in the experiments can be matched well with natural examples reported from Karonga basin, Malawi rift, Kenya.

Keywords Pervasive strength anisotropy · Orthogonal extension · Oblique extension · Strike-slip fault · Dip-slip fault · Oblique-slip fault

Introduction

Influence of preexisting basement anisotropy in the structural evolution of an extensional regime is now well established and is reported from many areas worldwide, e.g., from the East African Rift system (McConnell 1972; Daly et al. 1989; Hetzel and Strecker 1994; Ring 1994; Theunissen et al. 1996; Bellahsen et al. 2006), from the Tertiary rifts of Thailand (Morley et al. 2004), from the Paleozoic Gondwana rift basins of India (Chakraborty et al. 2003), from the North Coast transfer zone, Scotland (Wilson et al. 2010) from Makkovik Province,

Labrador, Canada (during opening up of the Labrador Sea, Peace et al. 2018), from the offshore West Greenland (Peace et al. 2017), and many others. The above examples reveal that the basement anisotropy of any form like a through-going, long, discrete fault, or an array of small isolated faults or even a penetrative metamorphic foliation or schistosity can considerably affect the evolution of structures, e.g., faults in a rift zone.

To have a better understanding of the role of preexisting anisotropy on structural evolution of an extensional regime, many workers have carried out experiments with analog models. Some of them have studied the role of preexisting en-echelon fractures in structural evolution under orthogonal and/or oblique extension viz. Thomas and Pollard (1993), Mandal (1995), An and Sammis (1996), Mauduit and Dauteuil (1996), Acocella et al. (1999), Bellahsen and Daniel (2005), Hus et al. (2005), Zwaan and Schreurs (2017), and Ghosh et al. (2019). Many workers have deformed precut analog models under single phase of extension.

✉ N. Ghosh
  ng1704@gmail.com

[1] Department of Geology, University of Delhi, Delhi 110007, India

Withjack and Jamison (1986), Serra and Nelson (1988), Tron and Brun (1991), Dauteuil and Brun (1993), McClay and White (1995), Clifton et al. (2000), and Corti et al. (2001) have studied the influence of a preexisting single, long, discrete fault under orthogonal and/or oblique extension at different angles. Morley (1999) has studied the evolution of normal faults under oblique extension, in presence of a preexisting anisotropy, using sand box models. Like other workers, working on similar problems, he has also used precut geometries in the underlying plates to impose preexisting fabrics on the developing fault system within the overlying material of isotropic strength. He has discussed that this type of model corresponds closely to a discrete and "active" type (movement along which directly produces the deformation) of preexisting fabric in nature. To more effectively model natural examples with preexisting "passive" (which undergoes deformation due to the movement along any other structural discontinuity) fabric, it should be the overlying layer (sand or clay cake) that contains the strength anisotropy. To address this problem (at least partially), Chattopadhyay and Chakra (2013) have studied the influence of pervasive anisotropy on the evolution of secondary fault patterns within a rift basin, using a different type of model. They have attempted to simulate anisotropy similar to metamorphic foliations or schistosity by applying brush marks within plaster of Paris layer. Upon extension in different angles, the brush marks behaved as strength anisotropy and guided the orientation and kinematics of the rift-related faults (e.g., dip-slip/oblique-slip normal fault, strike-slip link faults, etc.). They have found that if pervasive anisotropy exists at an angle greater than 45° w.r.t the maximum instantaneous horizontal stretching direction, new faults will form following them. Otherwise, they will disregard the anisotropy and will form perpendicular to the maximum instantaneous stretching direction.

Keep and McClay (1997), Bonini et al. (1997), Dubois et al. (2002), and Henza et al. (2011) have studied the deformation pattern of homogeneous model with two phases of extension. In their experiments, fractures/faults developed during 1st phase deformation act as anisotropy for the phase 2 deformation. The above mentioned works have clearly established that the preexisting fractures are reactivated only if they are suitably oriented with respect to the subsequent extension direction. If new faults are formed in a different direction, the preexisting faults can either act as a linking fault between them or even can block the propagation of them.

But there exist more complex natural situations where a zone with preexisting pervasive anisotropy experience successive phases of extensions in different directions (as described from the Malawi rift, Kenya by Ring 1994). In such cases which factor will control the formation of second phase faults is still not well studied. During the second phase of extensional deformation one or more of these can happen: (a) simply the phase 1 faults (either following or disregarding the preexisting anisotropy) can continue to grow, (b) new faults can form parallel to the phase 1 faults (either following or disregarding the anisotropy), or (c) new faults

can form along a different orientation, totally disregarding the preexisting faults and/or the mechanical anisotropy.

In the present work, analog models with pervasive anisotropy, similar to metamorphic foliations in basement gneisses and/or schists, are deformed by two successive phases of extensions. The main objective is to find out the relative influence of the pervasive anisotropy and of 1st generation faults on the formation of faults during the second phase of extension.

Experimental method

Deformation rig

The deformation rig (Fig. 1a) used in this experimental study consists of a base plate and two moving platens. One platen can move forward and backward resulting in an orthogonal compression or extension of the model respectively. The other platen can move parallel to its length, providing layer parallel (either sinistral or dextral sense) shear to the model. The movements of the two platens are controlled by two separate stepper motors. In case of orthogonal extension, only one platen moves away from the other creating a single VD and asymmetric extension. For oblique extension, both the platens move apart so that 2 VDs develop and the extension is more or less symmetrical. However, presence of single or double VD does not affect the result of deformation of the brittle-viscous three-layered models, as used in our experiments. This is due to the fact that the lower most viscous layer acts as a buffer that decouples the upper brittle layer from the base (Zwaan et al. 2019). Two metal plates (L-shaped in cross section) are attached one each with the two movable platens. One arm of the L-shaped plate is parallel to the platen, and the other is parallel to the base plate. These plates are capable of sliding over the base plate with movement of the platens. The face-to-face edges of these two plates meet with each other exactly along a central line, which represents the rift axis (Fig. 1b). A set of Cartesian axes is adopted as reference directions as shown in Fig. 1a. X-axis is parallel to the rift axis and Y-axis is parallel to the rift normal. The Z-axis is vertical. Velocities of both the platens can be varied between 0.2 and 2 mm/min. By changing the ratio of velocities of the platens the angle of extension/compression can be changed, thereby creating oblique extension/compression at different angles, as illustrated in Fig. 1c. The velocities of the platens set to get different angles of oblique extension are shown in (Table 1).

Modeling technique

Rectangular three-layered analog models (Fig. 2a) (≈ 24 cm × 15 cm × 4 cm) are used in the experiments as the representation of a rift zone. The base layer is made of soft pitch (80/100 bitumen from Indian Oil Corporation), capable of flowing
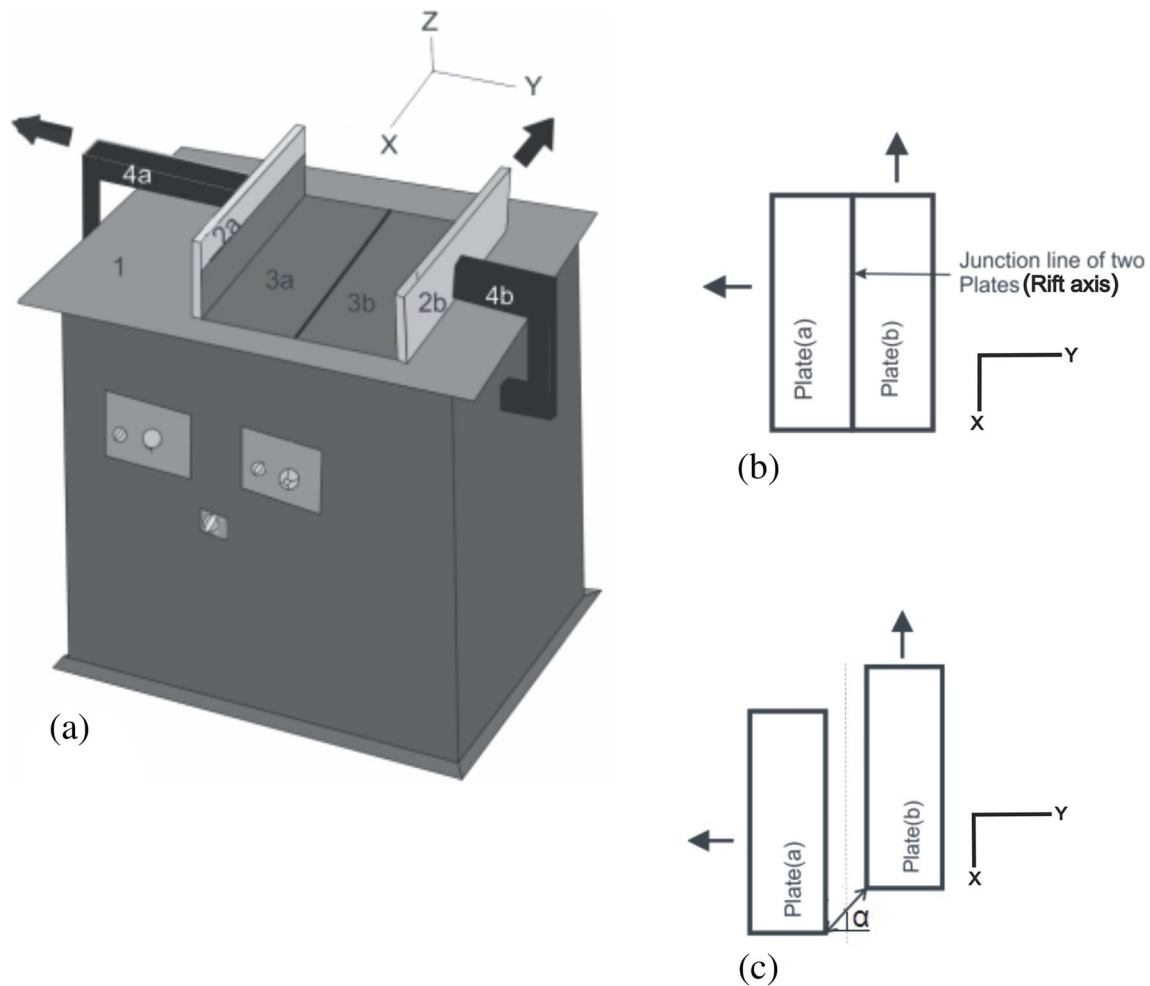
Fig. 1 a Deformation rig: 1, base plate; 2, moving platens (2a performs orthogonal and 2b performs sidewise movement); 3, L-shaped plates (3a attached with 2a and 3b attached with 2b); 4, rods attaching the platens with the respective motors. A set of Cartesian coordinates is shown as reference directions. **b** Initial position of the platens a and b (equivalent to 2a and 2b of **a**, respectively) (top view). Their junction represents the rift axis. **c** Position of the platens after a certain deformation (top view). Dotted line shows the direction of the rift axis. α = angle of oblique extension

slowly under its own weight. The rate of this flow is much less in comparison with the extension rate used in our experiments. So it does not affect our experimental results. The pitch layer (3 cm thick) is used to transfer the extensional stress created by the divergence of the basal plates to the upper brittle layer. The middle layer is of plaster of Paris (wet mixture of gypsum powder/water $\approx$ 3:1, volume/volume), and the top layer is made of dry, cohesionless sand. Wet plaster of Paris is spread over a rectangular block of pitch by brushing systematically along a desired direction with the help of a flat hard brush. After drying, these brush marks effectively represent small ridges and grooves (spacing between adjacent ridges or adjacent grooves is less than 2 mm, height of the ridges is approximately 0.4 cm) creating strength anisotropy in the plaster of Paris layer which is intended to produce the transverse strength anisotropy expected in vertically foliated metamorphic basement rocks. The relative strength contrast within Plaster of Paris layer (due to variation in thickness) is taken into account and not the exact value of strength of thicker and thinner layer. Dry quartz sand is sieved manually to make a 0.5-cm-thick layer over the pitch-plaster of Paris block. A square grid with sides parallel to X- and Y-axes (named x-marker and y-marker, respectively) is drawn on the top of the sand layer. A scale

Table 1 Different setups of the deformation rig

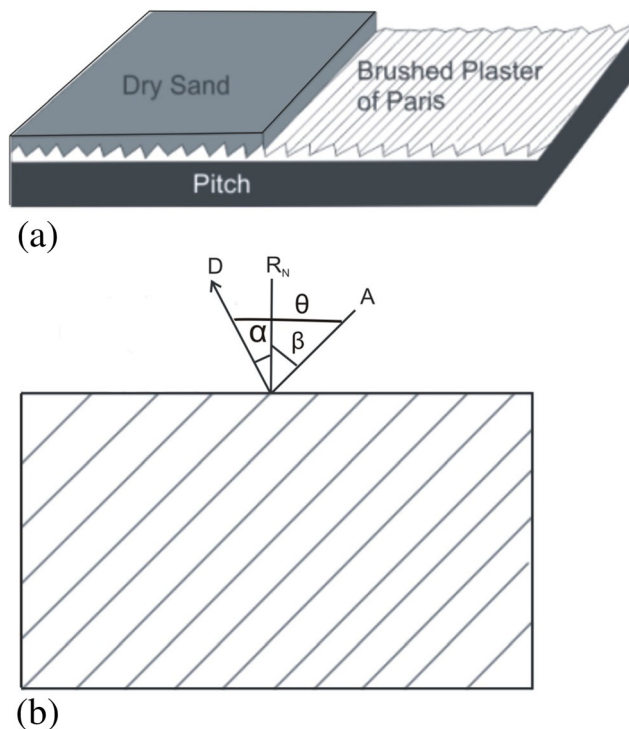| S.no	Angle of extension (α)	Velocity of plate a (mm/min)	Velocity of plate b (mm/min)	Resultant displacement between two adjacent point across the V.D (mm/min) (rate of divergence/effective extension velocity)
1	30°	1	0.5	1.1
2	0°	1	0	1

Fig. 2 **a** Schematic diagram of three-layered model (not to scale). Lower most pitch layer (thickness ≈ 3 cm), overlain by brushed plaster of Paris layer (thickness ≈ 0.5 cm) and at top is the layer of dry cohesion less sand (thickness ≈ 0.5 cm). **b** Schematic diagram of the top view of the model showing all the parameters. R_N = rift normal parallel to the Y direction of the Cartesian coordinate shown in Fig. 1a; α = angle of extension (with respect to R_N), D = direction of oblique extension, A = anisotropy, β = angularity of anisotropy (with respect to R_N), θ = angle between the extension direction and the anisotropy

representing 3 cm (divided into 3 segments each of 1 cm length) is placed on the upper left corner of the model.

Models are placed centrally above the rift axis with their length and width parallel to X- and Y-axes, respectively. The direction of extension w.r.t the Y-axis (rift normal: R_N), is designated as α. Many previous workers have followed this definition of α (e.g., Fournier and Petit 2007, Philippon et al. 2015, Brune 2016, Zwaan and Schreurs 2017, Ammann et al. 2018). However, many workers have also measured the angle α with respect to the rift axis (e.g., Tron and Brun 1991; Teyssier et al. 1995; Clifton and Schlische 2001; Chattopadhyay and Chakra 2013; Deng et al. 2018). We have represented the sinistral oblique extension by positive value of α. The orientation of the brush marks with respect to the Y-axis

(rift normal), measured clockwise, is designated as β (Fig. 2b). The angle between the extension direction and the brush mark is designated as θ. For orthogonal extension $\alpha = 0°$ and $\beta = \theta$. Each model is deformed by two successive phases of extensions (orthogonal and oblique). In series 1, orthogonal extension ($\alpha = 0°$) is followed by sinistral oblique extension ($\alpha = 30°$), and in series 2, sinistral oblique extension ($\alpha = 30°$) is followed by orthogonal extension ($\alpha = 0°$). Each phase of deformation is continued for 20 min. After completion of phase 1 extension (i.e., after an increase of approximately 10% in width of the model) about half of the top surface of the model is covered by red colored sand. This helps to recognize the initiation of new faults during the phase 2 extension. The changed width of the models (i.e., the dimension along Y-axis) is measured after each step. The value of longitudinal strain at each step is calculated as the ratio of change in the width to initial width. Four different types of models are made having four different directions of anisotropy (i.e., four different values of β, $\beta = 90°$, 60°, 45°, and 15°). The classification of the experiments according to different parameters is shown in the Table 2.

Model scaling

In our three-layered model, the lower most pitch block simulates viscous deformation of deep crustal rocks. The brushed plaster of Paris, which is brittle but relatively stronger than cohesionless sand, simulates the upper crustal, layered metamorphic rocks. The topmost dry sand pack stands for the upper most sedimentary rocks. The thickness of the pitch layer is around 3 cm, whereas that of plaster of Paris layer is around 0.5 cm and that of sand is around 0.5 cm. Thickness of (sand + plaster of Paris): pitch ratio is kept approximately 1:3 to simulate the ratio of brittle upper crustal layer (≈ 10 km) to viscous lower crustal layer (≈ 30 km).

Pitch (viscosity $\approx 1.5 \times 10^5$ Pa s at 25 °C) is an elastico-viscous material which flows as a non-Newtonian (power-law) viscous material under slow deformation and yields by brittle fracturing under faster loading rate. It is a suitably scaled material to simulate slow viscous deformation of the deeper part of the crust (e.g., Chattopadhyay and Mandal 2002; Chattopadhyay and Chakra 2013; Ghosh et al. 2014). The detailed calculation of scaling of pitch is given in the Appendix. The uppermost sedimentary layer is simulated by

Table 2 Different types of models	Experiments							
	Series 1 (1st phase orthogonal, 2nd phase oblique)				Series 2 (1st phase oblique, 2nd phase orthogonal)			
	A	B	C	D	A	B	C	D
	$\beta = 90°$	$\beta = 60°$	$\beta = 45°$	$\beta = 15°$	$\beta = 90°$	$\beta = 60°$	$\beta = 45°$	$\beta = 15°$

cohesionless, dry, quartz-rich sand (Coulomb rheology: angle of internal friction ≈ 31°, negligible tensile strength, density 1.5–1.7 g/cm³, average grain size ≈ 0.5 mm (Table 3)) (Davy and Cobbold 1988; Schön 2011; Chattopadhyay and Chakra 2013; Chattopadhyay et al. 2014). It is widely used in analog experiments to simulate brittle, upper crustal rocks, and is considered as scaled to nature (Tron and Brun 1991; Keep and McClay 1997; Bonini et al. 1997; Corti 2004; Corti et al. 2007). Though plaster of Paris is a brittle material with significant tensile strength (≈ 3 MPa), its tensile strength decreases sharply with porosity and thickness (Berenbaum and Brodie 1959; Nott 2009), and for a thin "corrugated sheet-like" layer as used in our experiments, it should be much lower. As we have no exact data at present on the tensile strength of such thin layers of plaster of Paris, dynamic scaling of our models remains somewhat uncertain. Brush marked plaster of Paris (similar to the models as used by Chattopadhyay and Chakra 2013) is however very suitable for simulating transverse strength anisotropy in brittle upper crustal rocks, which formed the main topic of our study. More importantly, its tensile strength is higher than that of the sand (≤ 100 Pa) so that a difference in strength between the "basement" and the "cover" rocks could be qualitatively simulated. The models thus made can be considered as "roughly scaled." The rheological properties of the materials are shown in Table 3.

The model materials which are used in the present work, at least roughly scale the experiments for a meaningful comparison with natural structures. Although the experimental deformation is kept as slow as possible (≈ 1 mm/min), time scaling

is not considered in this study as faulting/fracturing is a stress-sensitive, relatively fast process, and the strain rate is not essentially scaled for comparison with nature.

Observations

Series 1 (phase 1 orthogonal extension: $\alpha = 0°$, phase 2 oblique extension: $\alpha = 30°$)

Experiment 1A ($\beta = 90°$)

During phase 1 extension, anisotropy parallel, long, normal faults were formed at a longitudinal strain around $\lambda = 0.05$ (Fig. 3a). Small faults linking those long faults were developed at an angle between 150° and 160° with the anisotropy parallel faults at a longitudinal strain around $\lambda = 0.07$ (Fig. 3b). With increasing deformation, more new normal faults formed parallel to the anisotropy and all the normal faults continued to develop in the direction of extension. Maximum length of the isolated anisotropy parallel fault is around 13.3 cm. The orientations of the faults are graphically shown in Fig. 7a.

During phase 2 extension, the phase 1 normal faults started to develop as sinistral oblique fault (can be seen by offset of y-marker from its previous position, as marked by square B in Fig. 3d). New linking faults developed at a high angle (70° to 90°, measured anticlockwise) with the anisotropy. With increasing deformation, the new linking faults developed as dextral oblique fault (marked in Fig. 3f). The orientations of the faults are graphically shown in Fig. 7b. The schematic representation of the evolution of fault pattern due to two successive phases of extensions is given in Fig. 8a.

Table 3 Rheological properties of the materials used

|	Material	Density	Viscosity	Angle of internal friction	Tensile strength	Cohesion
1.	Dry sand	1.5–1.6 g/cc[a]		≈30°[b]	Negligible < 100 Pa	Nearly cohesionless
2.	Plaster of Paris (dried paste)	1.17 g/cc (of wet mixture)[c]		≈30.9°[d]	≈3 MPa for 1 cm thin disks (test on homogeneous material)[c]	≈13 MPa (compression test on homogeneous material)[d]
3.	Pitch	1.15 g/cc	1.5×10^5 Pa s at 25 °C[e]			

[a] Data source: Davy and Cobbold (1988)

[b] Data source: Keep and McClay (1997)

[c] Data source: Vekinis et al. (1993)

[d] Data source: Nott (2009)

[e] Data source: Jaeger (1969)

Fig. 3 Successive stages of deformation of model 1A, with increasing deformation from **a** to **f**. **a**–**c** Phase 1 deformation. **d**–**f** Phase 2 deformation. "A" represents the trend of anisotropy, "D" represents the extension direction, "R$_A$" represents rift axis, and "R$_N$" represents the rift normal. Sinistral oblique movement of anisotropy parallel phase 1 fault during phase 2 deformation is inferred from the sinistral offset of y-marker as shown by square B in **d**


(a)   (b)   (c)   (d)   (e)   (f)
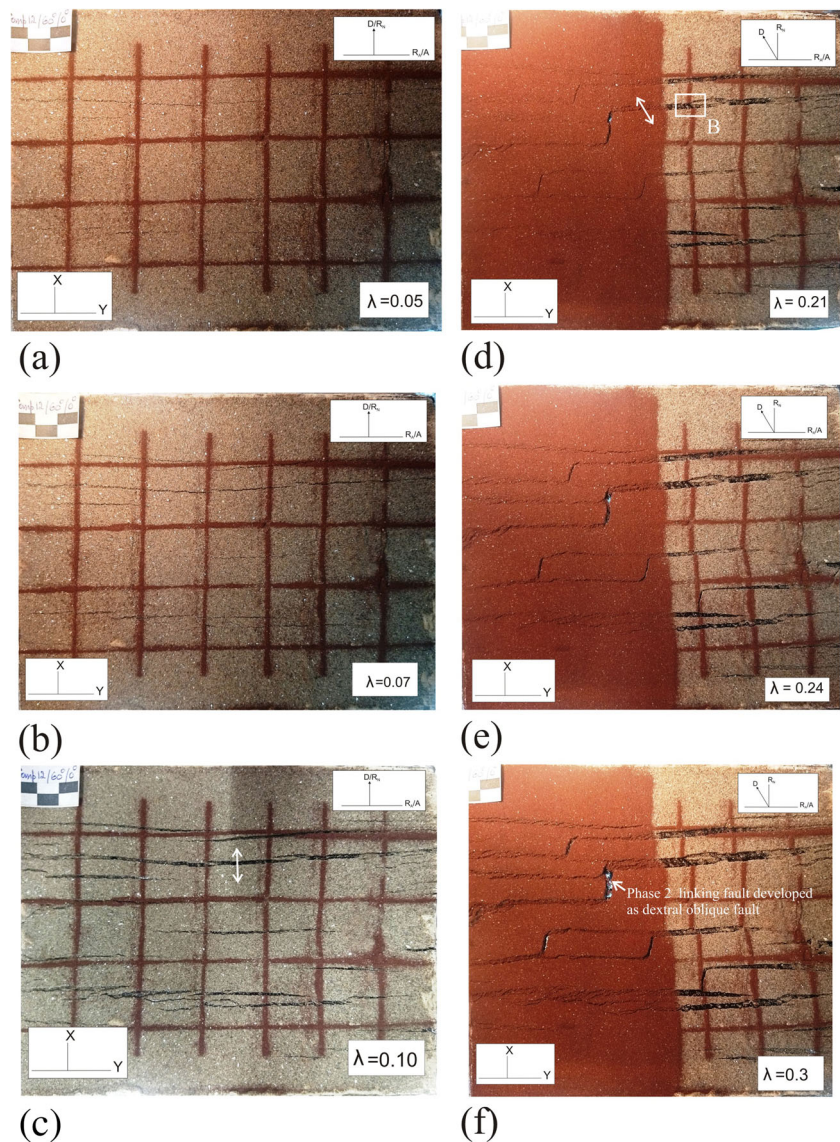
Experiment 1 B (β = 60º)

During phase 1 extension, anisotropy-parallel, oblique slip faults (i.e., at 60° angle with the rift normal) were formed at a longitudinal strain of $\lambda = 0.03$ (Fig. 4a). At a longitudinal strain of $\lambda = 0.05$, they were linked by two sets of small faults. The orientation of one set of linking faults was around 60°, and that of another set was around 110°, measured anticlockwise w.r.t the anisotropy-parallel faults (Fig. 4b). The anisotropy parallel faults grew as dextral oblique slip faults in the direction of extension. Maximum length of the isolated segment of those faults is 11.2 cm. The sense of movement along the fault was derived from dextral offset of the x-marker and moving apart of y-marker without any offset (shown by square B in Fig. 4c) across them. Linking faults oriented at 60° with respect to the anisotropy parallel fault grew as dextral

oblique faults whereas those oriented at an angle of 120° grew as sinistral oblique fault. The orientations of the faults are graphically represented in the Fig. 7c.

During phase 2 deformation, the anisotropy parallel phase 1 faults developed as dip-slip faults in the direction of extension. The sense of movement of these faults was supported by almost equal, but opposite-sense slip of two sets of markers (those were not offset during the phase 1 extension) as shown within square C of Fig. 4e. The x-marker showed a dextral sense offset, while the y-marker showed a sinsitral-sense offset. Some of those faults linked with each other by new linking faults (phase 2 linking faults) at around 60° (measured anticlockwise) giving rise to longer fault (Fig. 4e, f). The orientations of the faults are graphically represented in the Fig. 7d. The schematic representation of the evolution of fault pattern due to two successive phases of extensions is given in the Fig. 8b.

Fig. 4 Successive stages of deformation of Model 1B, with increasing deformation from **a** to **f**. **a–c** Phase 1 deformation. **d–f** Phase 2 deformation. "A" represents the trend of anisotropy, "D" represents the extension direction, "R$_A$" represents rift axis, and "R$_N$" represents the rift normal. Dextral oblique movement of anisotropy-parallel fault during phase 1 deformation is inferred from the dextral offset of x-marker and moving apart of y-marker without any offset, as marked by square B in **c**. Dip slip movement of the anisotropy parallel fault during phase 2 deformation is inferred from equal and opposite offset of two sets of markers as marked by square C in **e**
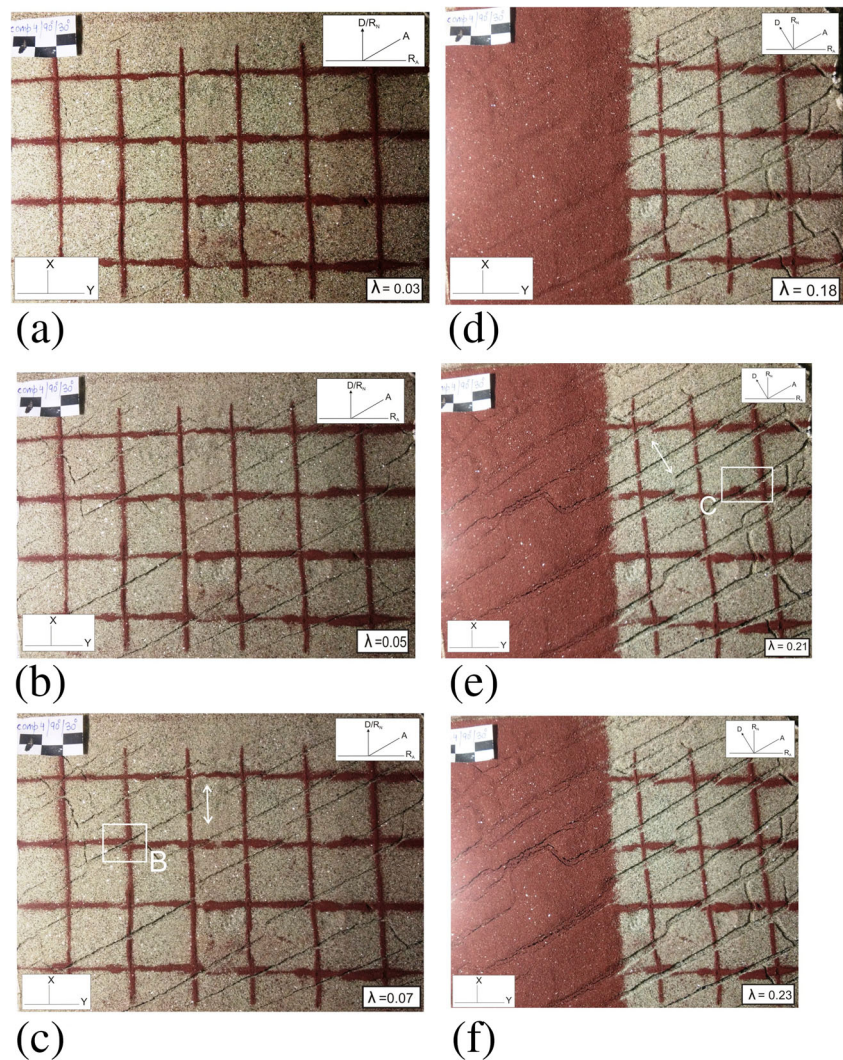
Experiment 1C (β = 45°)

During the phase 1 extension, anisotropy-parallel oblique slip faults and linking faults at an angle of 90° to 110° (measured anticlockwise) to them were formed simultaneously at a longitudinal strain λ = 0.04 (Fig. 5a). Both the sets of faults were of comparable length. Maximum length of the isolated segments of the anisotropy parallel faults is 6.4 cm. With continued extension, both set of faults developed in the direction of extension. New faults parallel to both the sets were formed (Fig. 5b, c). The linking faults developed as sinistral oblique slip faults. The sense of slip could be derived from the moving apart of y-marker across those faults, without any offset (as shown in square B in Fig. 5c). The anisotropy parallel faults developed as dextral oblique slip faults which is derived from the dextral offset of the x-markers across them (as shown in square C, Fig. 5c) and moving apart of y-markers

across these faults, without any offset (as shown in square D, Fig. 5c). The orientations of the faults are graphically shown in Fig. 7e.

During the phase 2 extension, both set of faults developed towards the direction of extension. Phase 1 anisotropy parallel faults continued to develop as dextral oblique faults (in contrast to the dip slip propagation of the anisotropy parallel phase 1 faults of model 1B) and that was derived from the shifting of markers (from their position after phase 1 deformation) in square E, Fig. 5f. On the other hand, the phase 1 linking faults developed up as sinistral oblique fault. At places new linking faults formed at much higher angle (around 130° to 140° measured anticlockwise, with the anisotropy parallel fault) coalescing both set of phase 1 small faults (Fig. 5e, f). The orientations of the faults are graphically shown in Fig. 7f. The schematic representation of the evolution of fault pattern due to two successive phases of extension is given in the Fig. 8c.

Fig. 5 Successive stages of deformation of model 1C, with increasing deformation from **a** to **f**. **a**–**c** Phase 1 deformation. **d**–**f** Phase 2 deformation. "A" represents the trend of anisotropy, "D" represents the extension direction, "R_A" represents rift axis, and "R_N" represents the rift normal. Sinistral sense of movement along linking faults during phase 1 deformation can be inferred from moving apart of y-marker without any offset as marked by square B in **c**. The dextral sense of movement of the anisotropy-parallel faults during phase 1 deformation can be inferred from the dextral offset of x-marker (as shown in square C, **c**) and moving apart of y-marker without any offset (as shown in square D, **c**). Dextral oblique movement of the anisotropy-parallel faults during phase 2 deformation can be inferred from the shifting of markers as shown in square E (**f**)
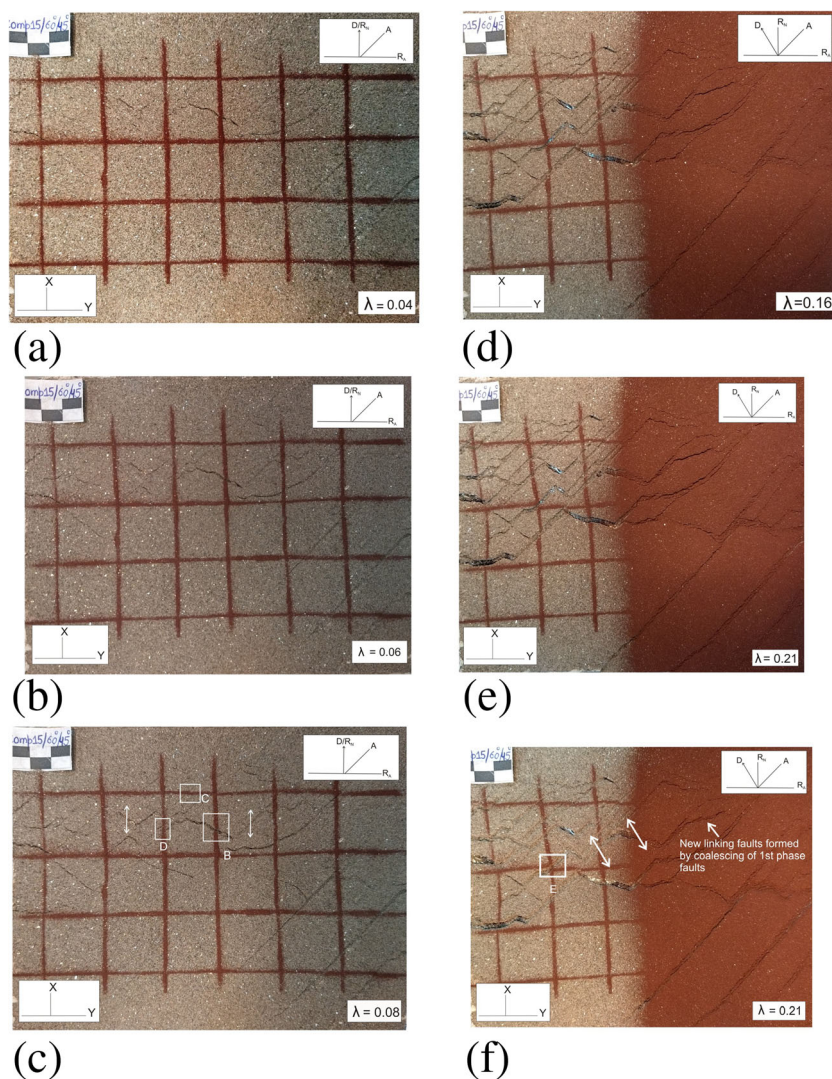
Experiment 1D (β = 15°)

During the phase 1 extension, small dip slip faults perpendicular to the extension direction (i.e., parallel to the rift axis) formed at longitudinal strain $\lambda = 0.07$, as major faults (Fig. 6a). They widely opened up and get linked by two other sets of faults. Those linking faults were developed disregarding the anisotropy. One set of linking faults was oriented at an angle of around 60° with the rift parallel faults (measured anticlockwise). Those faults were developed as dextral oblique faults with continued deformation. The other set of linking faults was oriented at an angle around 120° with the rift parallel faults (measured anticlockwise). Those faults developed as sinistral oblique faults with continued deformation. At a very late stage (at longitudinal strain $\lambda = 0.14$), prominent anisotropy parallel faults were formed and dextral slip took place along them as shown

by the slip of x-markers (square B, Fig. 6c). The maximum length of the isolated segments of the anisotropy parallel faults is 7.7 cm. The orientations of the faults are shown graphically in Fig. 7g.

During the phase 2 extension, the rift axis parallel faults started to develop as sinistral oblique slip fault (can be inferred from the shifting of markers as shown in square C, Fig. 6f). Numerous anisotropy parallel faults were also started to form. Gradually dextral oblique slip along them accommodated all the deformation and the rift axis parallel faults became inactive. At places, the anisotropy-parallel faults were linked by new faults at an angle of 150° (measured anticlockwise with them), cross cutting the rift axis parallel phase 1 faults. Some anisotropy parallel faults terminated at widely open rift axis parallel faults (basins) (Fig. 6f). The orientations of the faults are shown graphically in Fig. 7h. The schematic representation of the evolution of fault pattern due to two successive phases of extension is given in the Fig. 8d.

Fig. 6 Successive stages of deformation of model 1D, with increasing deformation from **a** to **f**. **a–c** Phase 1 deformation. **d–f** Phase 2 deformation. "A" represents the trend of anisotropy, "D" represents the extension direction, "R$_A$" represents rift axis, and "R$_N$" represents the rift normal. Dextral slip along the anisotropy-parallel faults during phase 1 deformation is shown by offset of x-markers as shown in square B (**c**). Sinistral movement of the rift axis parallel faults during phase 2 deformation is shown by offset of markers in square C (**f**)

(a) (b) (c) (d) (e) (f)
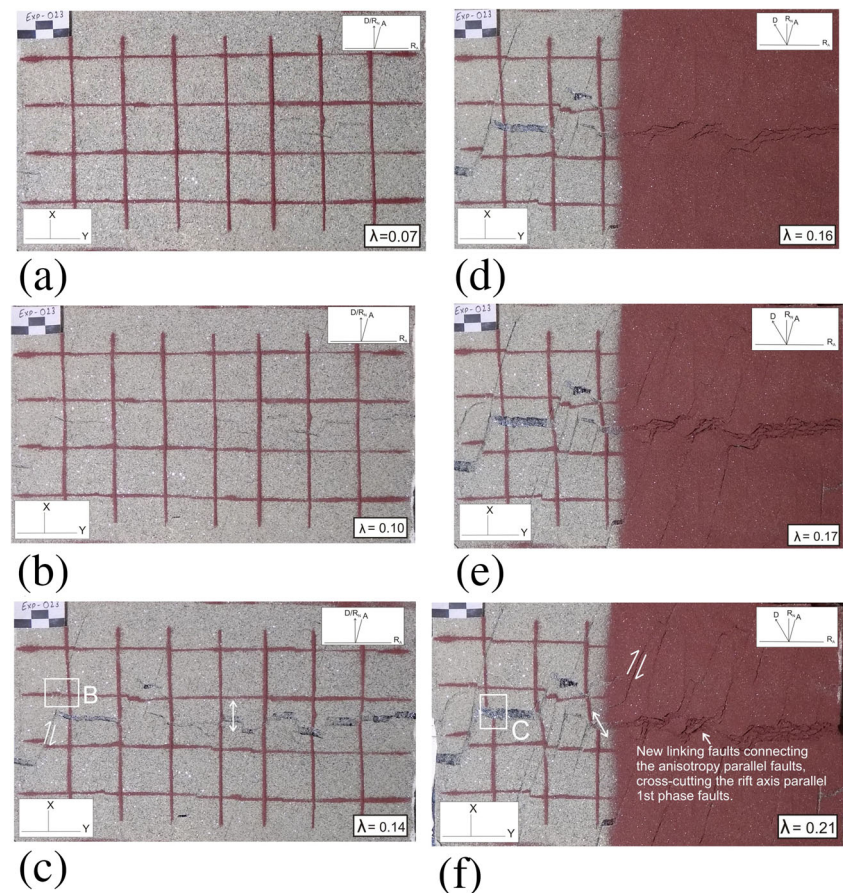
Series 2 (phase 1 oblique extension: $\alpha = 30°$, phase 2 orthogonal extension: $\alpha = 0°$)

Experiment 2A ($\beta = 90°$)

During phase 1 extension, anisotropy-parallel, long, oblique faults and linking faults almost perpendicular to the anisotropy-parallel faults, were formed almost simultaneously, at a longitudinal strain of $\lambda = 0.01$ (Fig. 9a). With continued deformation at a longitudinal strain of $\lambda = 0.03$, two sets of new linking faults, one set at 60° and the other set at 120° (measured anticlockwise) with respect to the anisotropy, were formed (Fig. 9b). New faults parallel to the direction of anisotropy were also formed and all the major faults continued to develop as sinistral oblique faults (deciphered from offset of y-marker as marked by square B in Fig. 9c). Maximum length of isolated segment of anisotropy parallel fault is around 10.5 cm. The orientation of the faults is graphically represented in the Fig. 13a.

During phase 2 extension, anisotropy parallel oblique faults started to develop as normal faults (Fig. 9d). Some new linking faults at 60°, 90°, and 120° (measured anticlockwise) with respect to the anisotropy were formed (Fig. 9f). The orientation of the faults is graphically represented in the Fig.
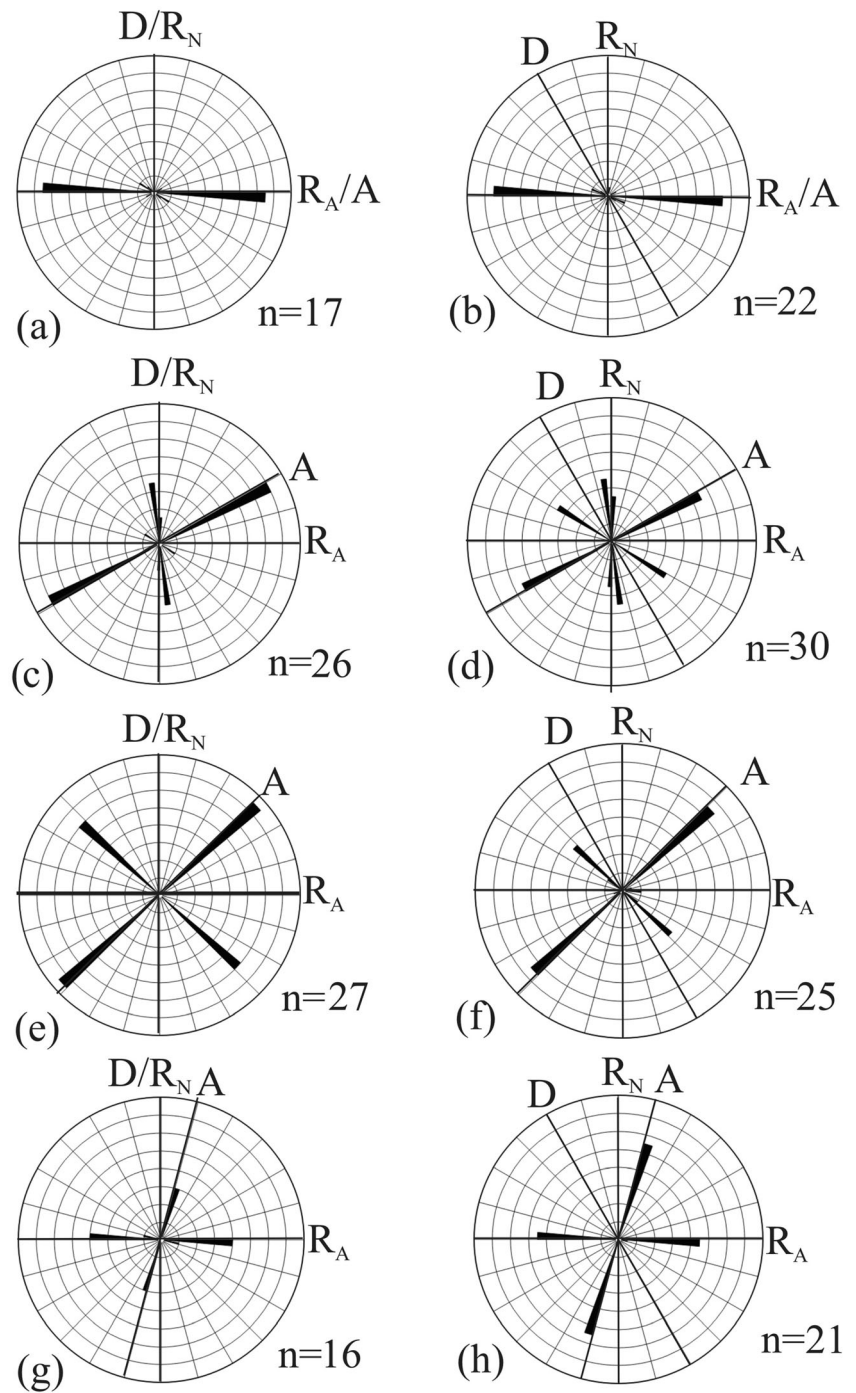
13b. Schematic representation of the development of fault patterns is represented in Fig. 14a.

Experiment 2B ($\beta = 60°$)

During the phase 1 extension, long anisotropy-parallel dip slip faults were formed at a longitudinal strain of $\lambda = 0.04$ (Fig. 10a). No other set of faults were developed. Anisotropy parallel faults developed as pure dip slip faults (inferred from almost equal offset of x- and y-markers, shown in square B, Fig. 10c) in the direction of extension. The maximum length of the isolated segments of those faults is 22.3 cm. The orientations of the faults are shown graphically in Fig. 13c.

During phase 2 of extension the anisotropy parallel faults started to slip in the new direction of extension. Thus, the phase 1 dip slip fault reactivated as dextral oblique slip fault (inferred from the dextral offset of the x-marker and moving apart of y-marker without any separation, which were not offset during the phase 1 extension) (shown in square C, Fig. 10f). At a longitudinal strain of $\lambda = 0.29$, two sets of linking faults were formed: one set perpendicular to the extension direction and the other set almost perpendicular to the major fault

(Fig. 10f). The linking faults perpendicular to the extension direction were very few in numbers and did not continue to develop with increasing deformation. The linking faults, almost perpendicular to the anisotropy-parallel faults developed as sinistral oblique faults. The orientations of the faults are shown graphically in Fig. 13d. The schematic representation of the evolution of fault pattern due to two successive phases of deformation is given in the Fig. 14b.

Experiment 2C (β = 45°)

During the phase 1 extension, long anisotropy-parallel oblique slip faults were formed (at longitudinal strain of $\lambda = 0.04$) (Fig. 11a). At longitudinal strain $\lambda = 0.05$, linking faults started to form at 90° to 110°, measured anticlockwise with the anisotropy parallel faults (Fig. 11b). The anisotropy-parallel faults developed as dextral oblique- slip fault (inferred from the dextral offset of x-marker as marked in square B, Fig.
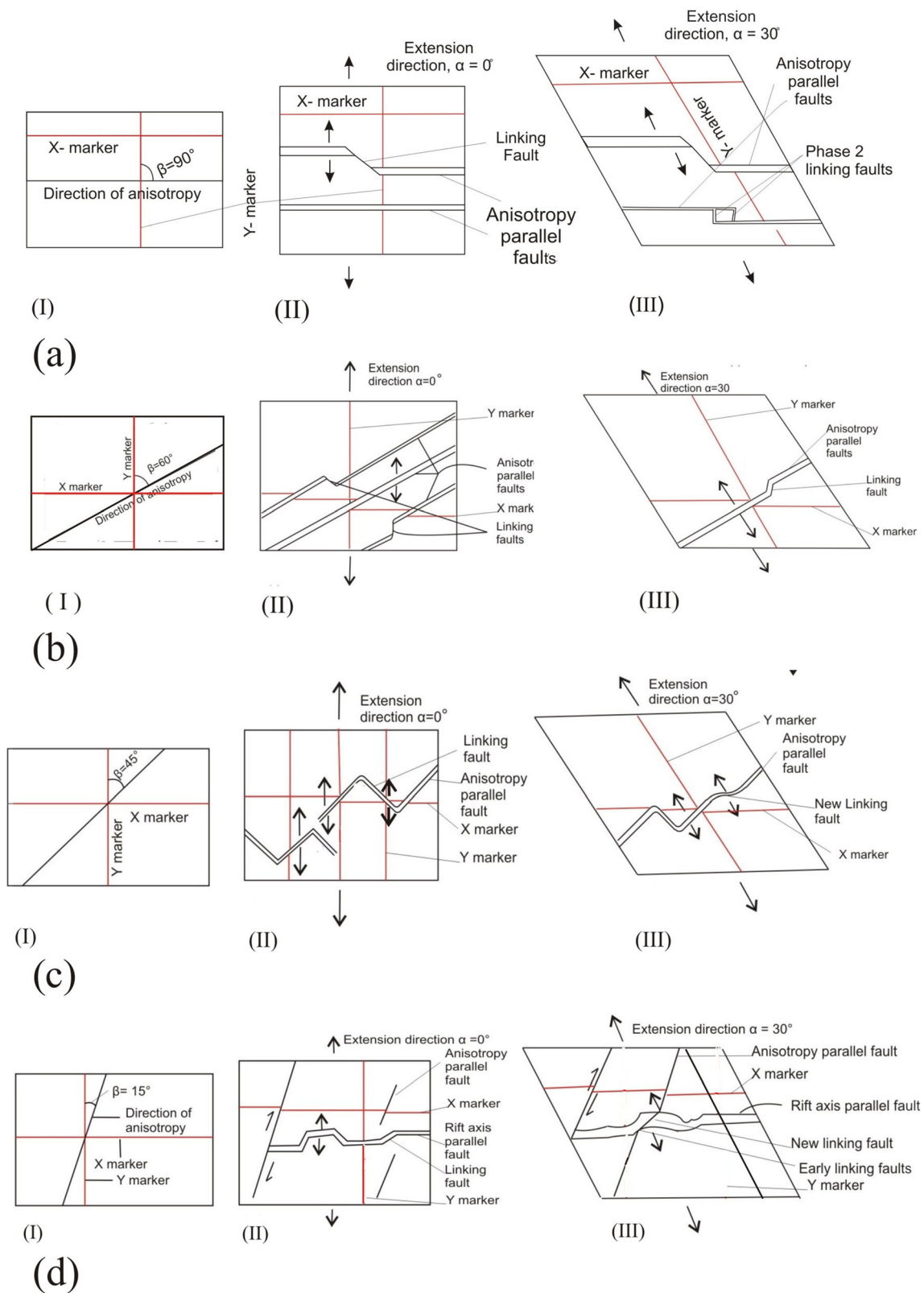
Fig. 8 Schematic diagram showing the development of fault patterns during two successive stages of deformation of series 1 models. **a** Model 1A—(I) initial stage, (II) stage after phase 1, (III) stage after phase 2. **b** Model 1B—(I) initial stage, (II) stage after phase 1, (III) stage after phase 2. **c** Model 1C—(I) initial stage, (II) stage after phase 1, (III) stage after phase 2. **d** Model 1D—(I) initial stage, (II) stage after phase 1, (III) stage after phase 2

Fig. 9 Successive stages of deformation of model 2A, with increasing deformation from **a** to **f**. **a**–**c** Phase 1 deformation. **d**–**f** Phase 2 deformation. "A" represents the trend of anisotropy, "D" represents the extension direction, "R$_A$" represents rift axis, and "R$_N$" represents the rift normal. Sinistral oblique movement of the anisotropy parallel faults can be deciphered from the offset of y-marker as shown by square B (**c**)
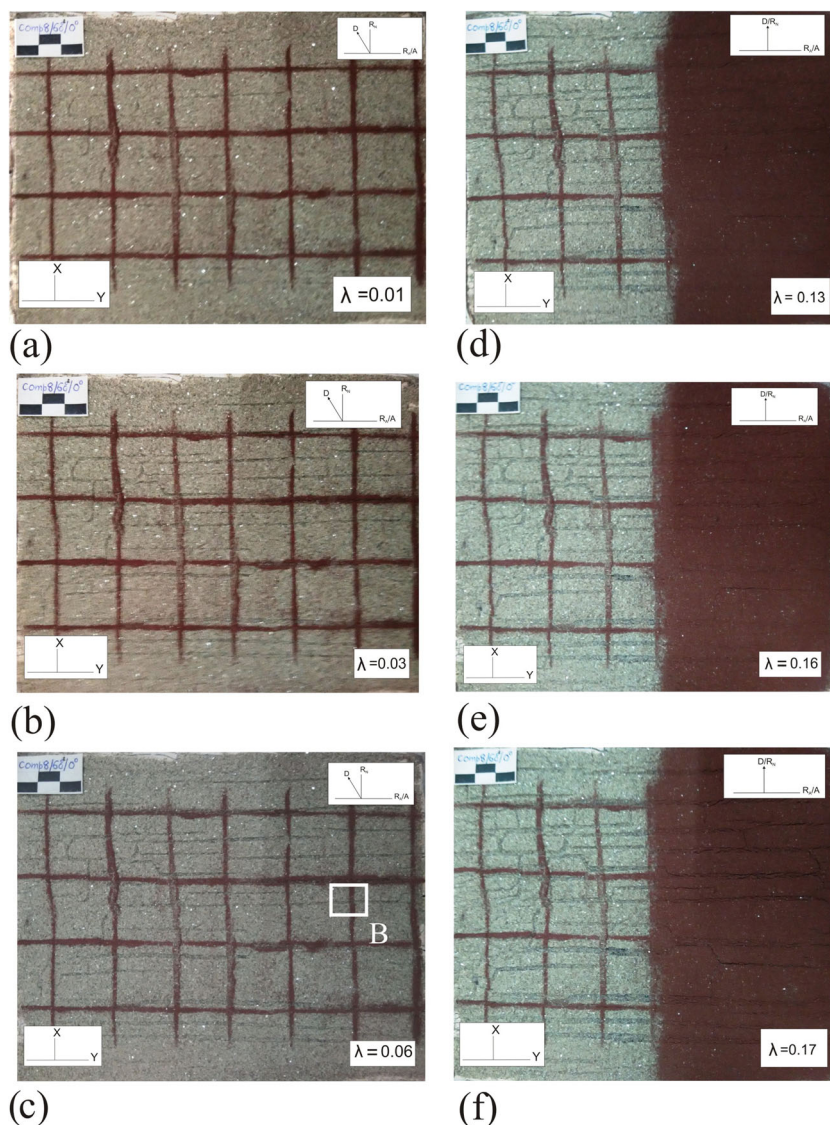
11c). The maximum length of isolated segments of those faults is 21.4 cm. The orientations of the faults are shown graphically in Fig. 13e.
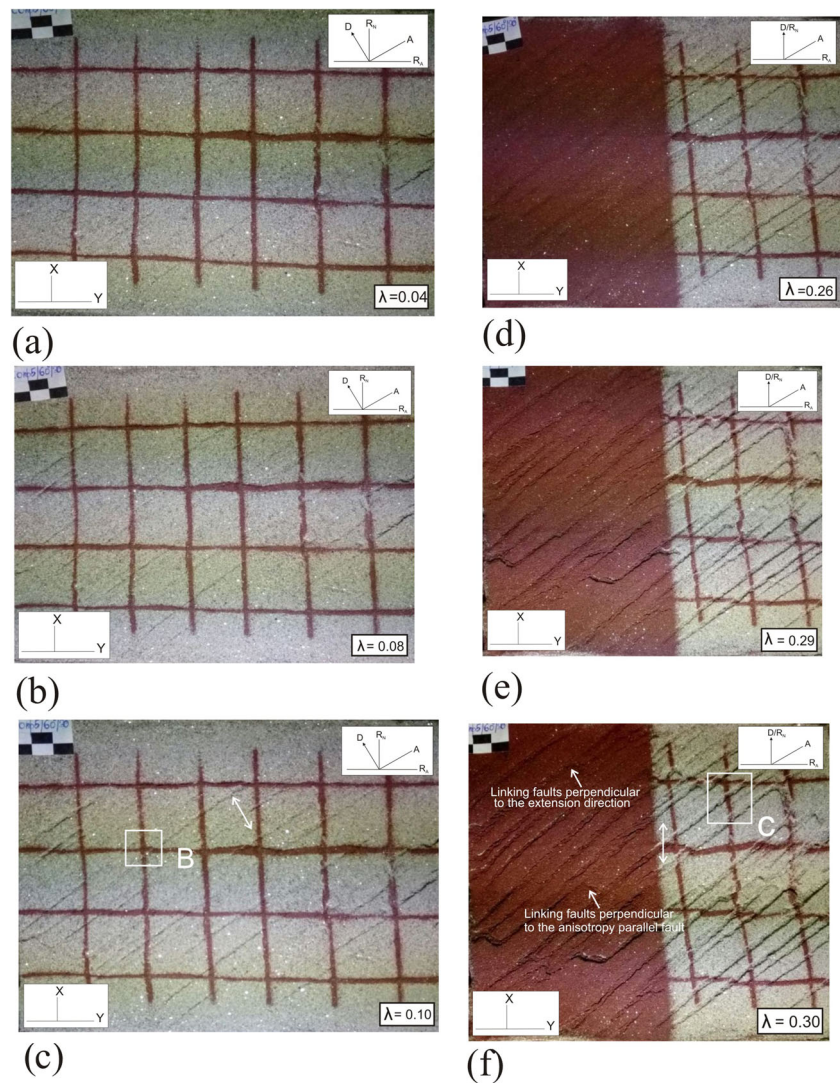
During phase 2 extension, anisotropy parallel faults underwent slip in the new direction of extension. Thus, the phase 1 dextral oblique faults continued to develop as dextral fault during the phase 2 extension. New (phase 2) linking faults developed mostly at around 120°, measured anticlockwise with the anisotropy parallel faults (marked in Fig. 11e). Those faults were developed as sinistral oblique faults with continued deformation. A few phase 2 linking faults were also formed perpendicular to the extension direction (marked in Fig. 11e). However, those faults were very few in numbers and their development was negligible during phase 2 extension. The orientations of the faults are shown graphically in Fig. 13f. The schematic representation of the evolution of fault pattern due to two successive phases of deformation is given in the Fig. 14c.

Experiment 2D (β = 15°)

During phase 1 extension, numerous anisotropy-parallel faults were formed at $\lambda = 0.04$ (Fig. 12a). At longitudinal strain $\lambda \approx 0.08$, numerous linking faults at 90° to 100°, measured anti-clockwise with them started to form (Fig. 12b). Dextral slip took place along the anisotropy parallel faults. This can be inferred from the dextral offset of x-markers as shown by square B in Fig. 12c. The maximum length of isolated segment of the anisotropy parallel faults is 10.2 cm. The orientations of the faults are shown graphically in Fig. 13g.

During phase 2 extension initially (up to longitudinal strain $\lambda \approx 0.15$), the linking faults remained active and developed as sinistral oblique faults. New faults parallel to the linking faults were formed and developed similarly (Fig. 12d). From longitudinal strain $\lambda \approx 0.17$, existing anisotropy-parallel faults started to become longer and new anisotropy-parallel faults started to form. Dextral slip along them became more

Fig. 10 Successive stages of deformation of model 2B, with increasing deformation from **a** to **f**. **a–c** Phase 1 deformation. **d–f** Phase 2 deformation. "A" represents the trend of anisotropy, "D" represents the extension direction, "R$_A$" represents rift axis, and "R$_N$" represents the rift normal. Dip slip movements of the anisotropy parallel faults during phase 1 deformation is inferred from the equal and opposite offset of x- and y-markers as shown in square B (**c**). Dextral oblique sense of the movement of the anisotropy parallel faults during phase 2 deformation can be inferred from the slip of the markers as shown in square C (**f**)

Discussion

Initiation and development of phase 1 faults

For phase 1 orthogonal extension (series 1), faults formed following the anisotropy for $\beta = 90°$, 60°, and 45° (e.g., experiments 1A, 1B, 1C, Figs. 3a–c, 4a–c, and 5a–c). For $\beta = 15°$, the faults formed perpendicular to the extension direction

dominant than the opening up of the linking faults (Fig. 12e). Gradually, the 1st phase linking faults became inactive and the anisotropy parallel faults crosscut them. The boundaries of the 1st phase linking faults were sheared along those anisotropy-parallel faults (as shown in square C, Fig. 12f). The orientations of the faults are shown graphically in Fig. 13h. The schematic representation of the evolution of fault pattern due to two successive phases of deformation is given in the Fig. 14d.

disregarding the anisotropy (e.g., experiment 1D, Fig. 6a–c), but a few anisotropy-parallel faults also formed at a very late stage of extension. For oblique extension, i.e., when the far-field stress had a shear component, the faults initiated following the anisotropy for all values of β (e.g., experiments 2A, 2B, 2C, 2D, Figs. 9a–c, 10a–c, 11a–c, and 12a–c). Thus, mode of far-field stress has a control on the phase 1 fault initiation in rocks with pervasive strength anisotropy. For $\beta = 15°$, anisotropy-parallel faults grew as strike slip faults regardless of the far-field extension direction (experiments 1D, 2D, Figs. 6a–c and 12a–c). By comparing the schematic diagrams represented in Fig. 8d(II) and Fig. 14d(II), it can be seen that the anisotropy-parallel faults are developing as strike slip faults in spite of the models undergoing different directions of extensions. In case of oblique extension their sense of slip (dextral) was opposite (experiment 2D, Figs. 12a–c) to that of the far-field sinistral shear sense. So, in this case, they can be compared to antithetic Riedel shears as they were oriented at too high an angle with the rift axis. For $\beta = 45°$, 60° and $\beta =$

Fig. 11 Successive stages of deformation of model 2C, with increasing deformation from **a** to **f**. **a–c** Phase 1 deformation. **d–f** Phase 2 deformation. "A" represents the trend of anisotropy, "D" represents the extension direction, "R_A" represents rift axis, and "R_N" represents the rift normal. The dextral oblique sense of slip of the anisotropy-parallel faults during phase 1 deformation can be inferred from the shifting of markers as shown by square B in (**c**)
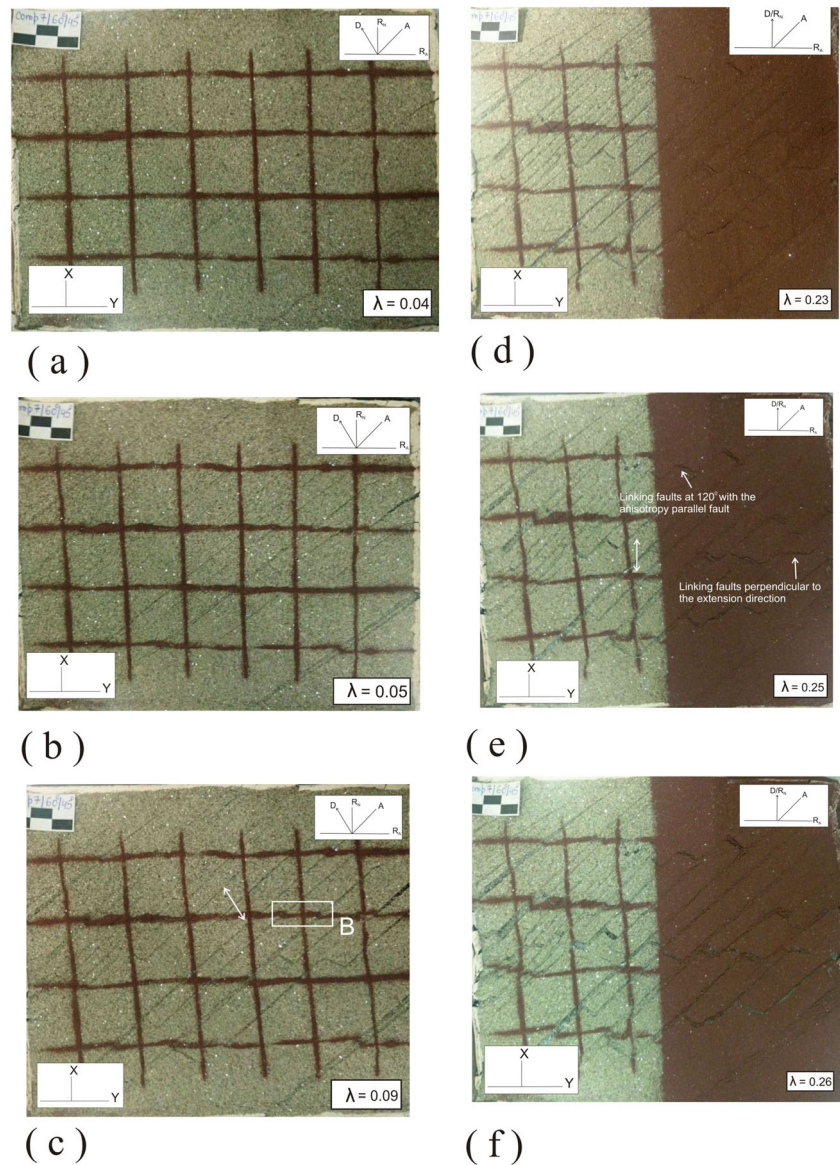
90°, the faults developed towards the direction of extension as either dip slip (experiment 1A, 2B, Figs. 3a–c and 10a–c, as shown in schematic diagram Fig. 8a(II) and Fig. 14b (II)) or oblique slip faults (experiments 1B, 1C, 2A, 2C, Figs. 4a–c, 5a–c, 9a–c, and 11a–c, as shown in schematic diagrams Fig. 8b(II), Fig. 8c(II), Fig. 14a(II), Fig. 14c(II)). Thus, the growth of faults having low obliquity with the rift normal ($\beta = 15°$) is not controlled by the direction of extension (at least when the direction of extension is at an angle $\leq 45°$ with them) whereas that of the faults more oblique ($\beta = 45°$, $\beta = 60°$) or orthogonal to the rift normal is controlled by the direction of extension vector.

Under orthogonal extension, initiation of faults following the anisotropy for $\beta = 45°/60°/90°$ and perpendicular to the extension direction, disregarding the anisotropy for $\beta = 15°$, matches well with the proposal of Chattopadhyay and Chakra

(2013). But under oblique extension, we have found that the faults initiate following the anisotropy even for $\beta = 15°$, which is in contrast to the proposal of Chattopadhyay and Chakra (2013). This may be due to the fact that in presence of a shear component, this value of β is more favorable for the formation of antithetic Riedel fractures than formation of new faults crosscutting the anisotropy.

Length of anisotropy-parallel phase 1 faults

From the data of the length of anisotropy parallel phase 1 faults (Fig. 15), it is observed that the fault length is controlled by their orientation (θ) with respect to the extension direction rather than their orientation (β) with respect to the rift normal. Longer faults are formed for higher value of θ, even if the value of β is the same. For example, the series 2 models with

Fig. 12 Successive stages of deformation of model 2D, with increasing deformation from **a** to **f**. **a–c** Phase 1 deformation. **d–f** Phase 2 deformation. "A" represents the trend of anisotropy, "D" represents the extension direction, "R_A" represents rift axis, and "R_N" represents the rift normal. The dextral slip along the anisotropy-parallel faults during phase 1 deformation can be inferred from the offset of markers shown by square B (**c**). Sheared boundary of phase 1 linking faults by anisotropy parallel faults is shown in square C (**f**)
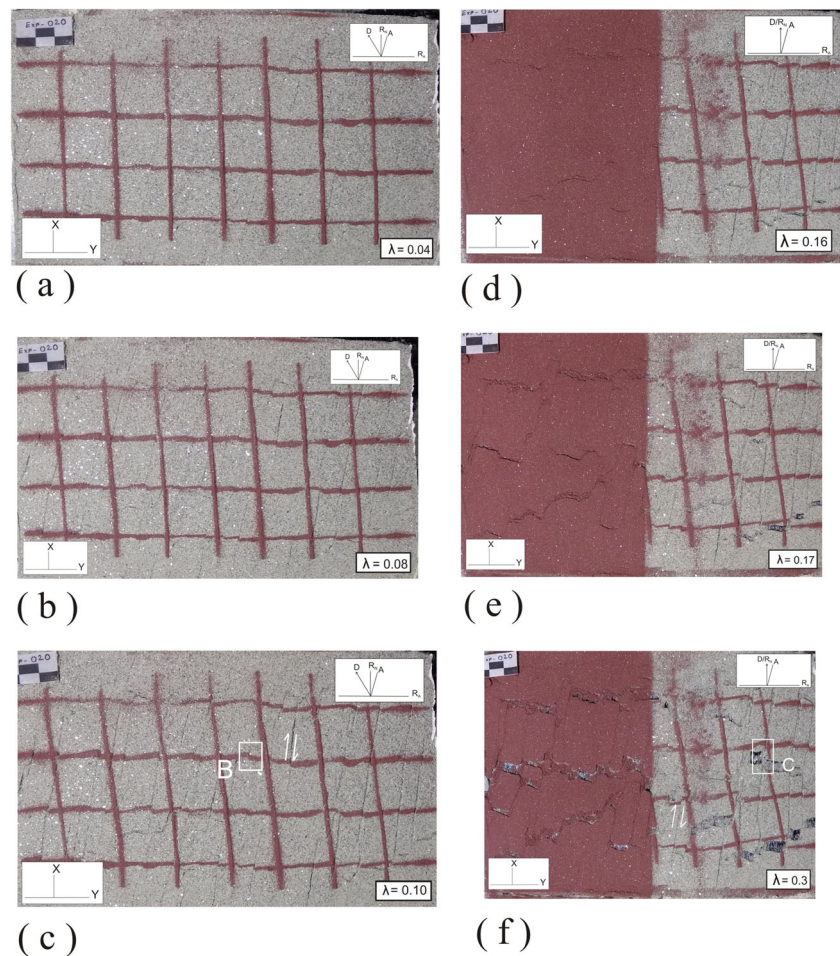
oblique anisotropy have longer faults than their series 1 counterparts as the former have higher value of θ. However, for orthogonal anisotropy, the series 1 model has longer fault due to the same fact. Similar variation in fault length is also described by Agostini et al. 2011 from their experimental study and natural fault patterns of Main Ethiopian Rift.

Such variation in fault length may happen due to the fact that with decreasing angle with respect to the extension direction the shear component along the fault increases. Increasing shear component favors the curvature of tip towards the adjacent fault, thus favoring more segmentation and formation of smaller faults.

Fault pattern during phase 2 extension

The phase 1 faults develop actively during phase 2 extension only if they are formed parallel to the direction of anisotropy. The phase 1 faults formed following the orthogonal and/or more oblique anisotropy ($\beta = 45°$, 60°) develop actively in the direction of phase 2 extension. Thus the phase 1 oblique faults may reactivate as dip slip faults (experiments 1B, 2A Figs. 4d–f and 9d–f), phase 1 dip slip faults may reactivate as

oblique slip faults (experiments 1A, 2B, Figs. 3d–f and 10d–f) or phase 1 oblique slip faults may continue to develop as oblique slip faults (experiments 1C, 2C, Figs. 5d–f and 11d–f) with different amount of oblique component. The less oblique ($\beta = 15°$) anisotropy-parallel phase 1 faults reactivate as strike slip faults irrespective of the direction of phase 2 extension (experiments 1D, 2D, Figs. 6d–f and 12d–f). Figure 16 schematically shows the pattern of reactivation of phase 1 faults during phase 2 extension. The less oblique fault AB ($\beta = 15°$) reactivates as strike slip fault irrespective of the direction of extension (as shown in Fig. 16 a, b). The fault CD ($\beta = 45°$) reactivates as more oblique fault under phase 2 orthogonal extension (Fig. 16a) than phase 2 oblique extension (Fig. 16b). The fault EF ($\beta = 60°$) reactivates as oblique fault under phase 2 orthogonal extension (Fig. 16a) but as dip slip fault under phase 2 oblique extension (Fig. 16b).

Many earlier workers (Keep and McClay 1997; Bonini et al. 1997; Henza et al. 2011) have mentioned that the fault pattern during the phase 2 extension will be strongly influenced by the phase 1 faults. However, they have not considered the role of preexisting, strong,

Fig. 13 Rose diagrams showing orientations of faults of series 2 models. *A* = the anisotropy, *D* = the extension direction, *R$_N$* = the rift normal, *R$_A$* = rift axis, and *n* = number of data measured. Bin size = 15. Frequency interval between each concentric circle = 2. **a** Faults after phase 1 deformation of model 2A. **b** Faults after phase 2 deformation of model 2A. **c** Faults after phase 1 deformation of model 2B. **d** Faults after phase 2 deformation of model 2B. **e** Faults after phase 1 deformation of model 2C. **f** Faults after phase 2 deformation of model 2C. **g** Faults after phase 1 deformation of model 2D. **h** Faults after phase 2 deformation of model 2D
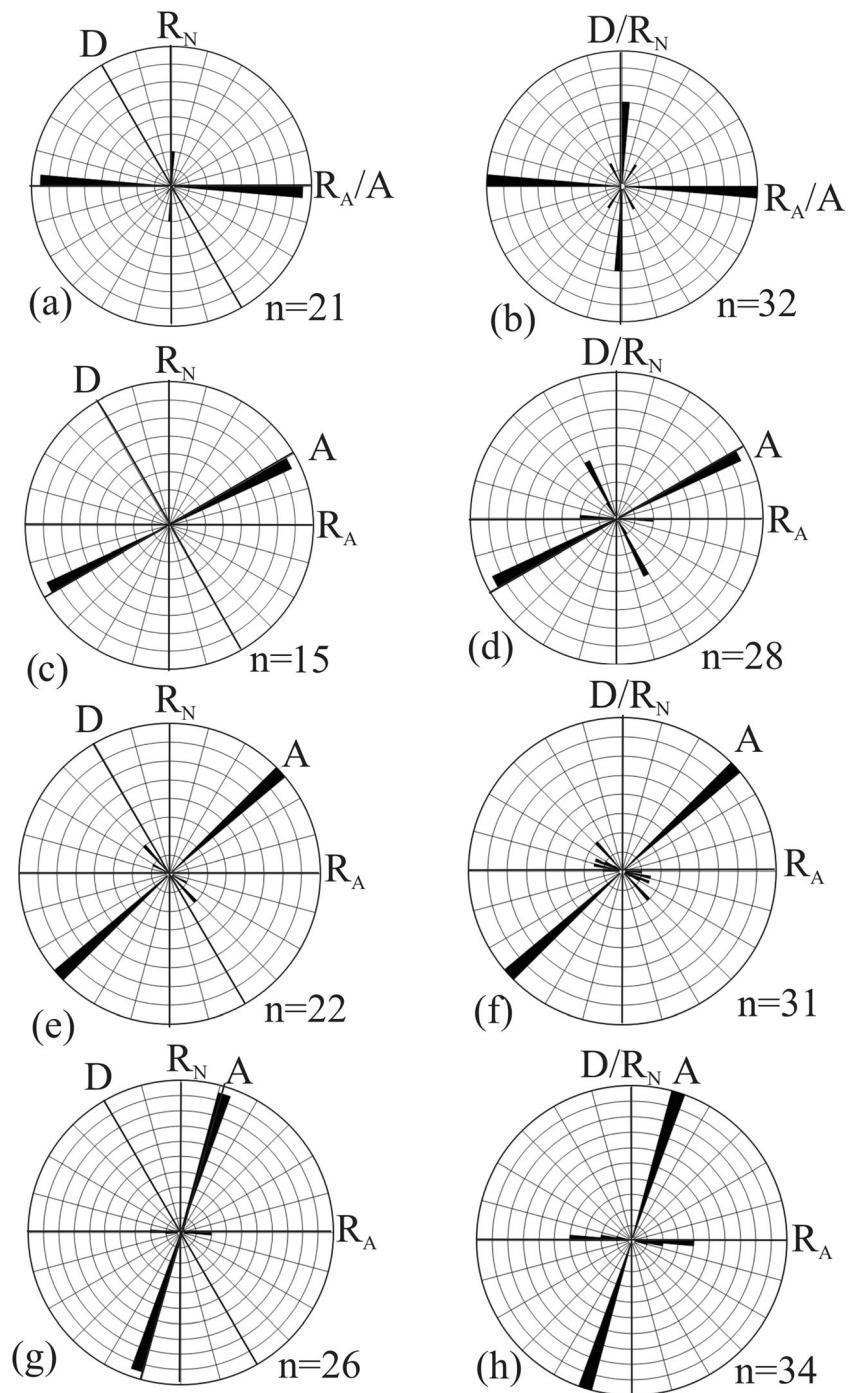
pervasive anisotropy in controlling the deformation. From our experiments, we can say that the phase 1 faults control the phase 2 deformation (by moving actively and/or facilitating formation of new faults parallel to them) only when they are parallel to the preexisting pervasive anisotropy. The major faults formed disregarding the anisotropy during phase 1 deformation become almost inactive during the phase 2 extension. New faults form parallel to the pervasive anisotropy

and accommodate almost all the deformation during phase 2 (experiment 1D, Fig. 6d–f). Phase 1 linking faults also do not able to accommodate much deformation even if they are more favorably oriented with respect to the phase 2 extension direction than the pervasive anisotropy parallel faults (experiment 2D, Fig. 12d–f). Thus, the preexisting pervasive anisotropy (provided that it is strong enough to influence the deformation) has a greater control than the phase 1

Fig. 14 Schematic diagram showing the development of fault patterns during two successive stages of deformation of series 2 models. **a** Model 2A—(I) initial stage, (II) stage after phase 1, (III) stage after phase 2. **b** Model 2B—(I) initial stage, (II) stage after phase 1, (III) stage after phase 2. **c** Model 2C—(I) initial stage, (II) stage after phase 1, (III) stage after phase 2. **d** Model 2D—(I) initial stage, (II) stage after phase 1, (III) stage after phase 2
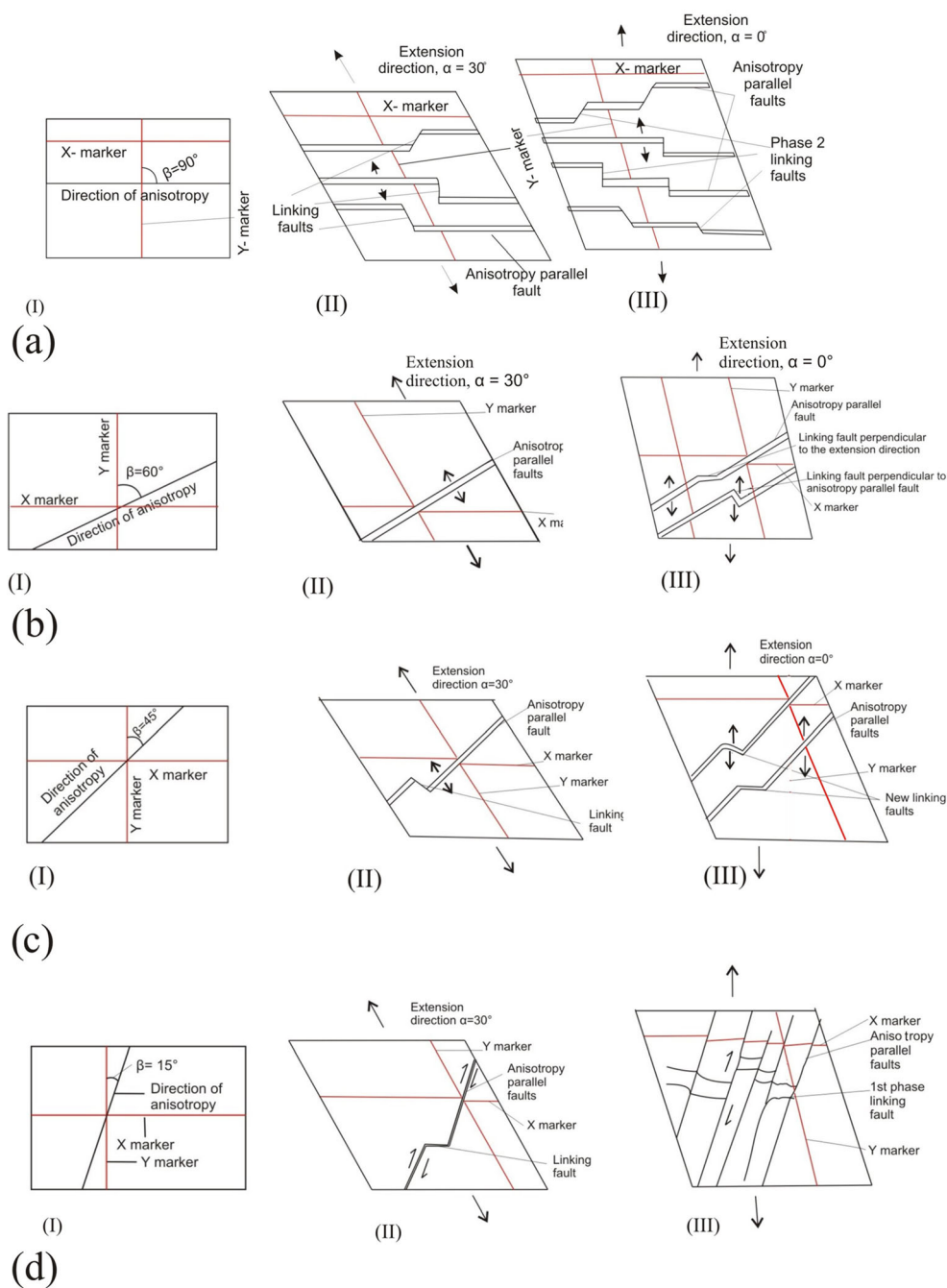
discrete faults in the development of final fault pattern in multiple phases of extension.

Comparison of experimental results with natural example

The results obtained from our experiments can be well compared with the natural examples of fault patterns as observed in Karonga Basin (also known as North Basin), northern Malawi Rift, Africa (Fig. 17a, b) (Ring 1994). During Cenozoic rifting, due to initial ENE-WSW orthogonal extension, dip slip faults are formed in the western part of Karonga basin (marked by square C in Fig. 17b). These faults cross cut the basement foliations within Precambrian Mugesse shear zone (Fig. 17c), similar to the phase 1 results of our experiment 1D. However, during 2nd phase of extension in the WNW-ESE direction, transfer faults (oriented SE, ESE, E, and ENE) are formed following the underlying basement shear zone foliations (Fig. 17d). The result of phase 2 extension of our experiment 1D can be compared well with the formation of transfer

Fig. 15 Graph of fault length vs. fault orientation with respect to the extension direction. Fault length (l) is plotted along *Y*-axis and the angle between the extension direction and anisotropy parallel faults (*θ*) is plotted along *X*-axis
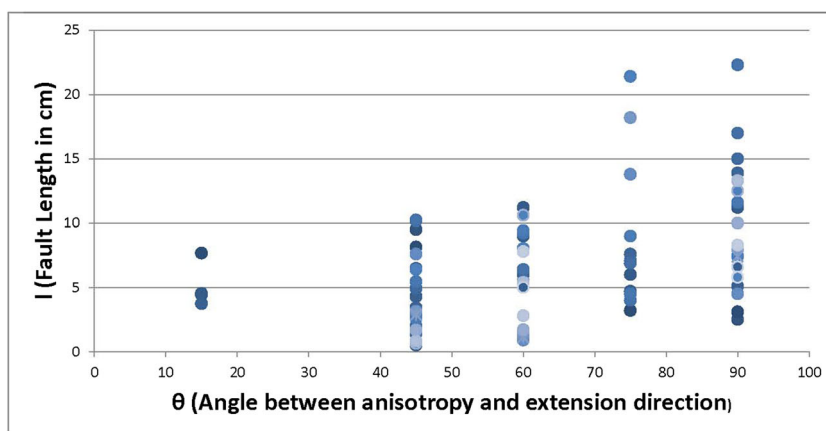
faults following the direction of ENE foliation under WNW-ESE extension.

In the Eastern part of the basin (marked by square D in Fig.17b), during initial ENE-WSW orthogonal extension, the Livingstone Border fault was initiated as a dip slip reactivation of the dominant foliation of the underlying Precambrian shear zone (Fig. 17e). During later WNW-ESE extension, the Livingstone Border Fault was reactivated as dextral strike slip fault (Fig. 17f). The results of our experiment 1A can be compared well with this example.

Conclusions

The above experimental work was done to study the role of preexisting pervasive anisotropy (strong enough to influence the deformation) in the development of fault patterns during two successive phases of extension. Analog models with

pervasive anisotropy, intended to represent a rift zone with a foliated metamorphic basement were used. The different orientations of the pervasive anisotropy with respect to the rift normal were set at $\beta = 15°$, 45°, 60°, and 90°. The models were deformed by either orthogonal extension followed by sinistral oblique extension at 30° with the rift normal or vice versa. From the results obtained, the following conclusions can be made-

1. Mode of far-field bulk deformation of the rift system has a control on fault initiation. Presence of shear component in the far-field stress favors initiation of antithetic strike slip faults following the less oblique anisotropy rather than extensional faults crosscutting that anisotropy.

2. The phase 1 faults reactivate during the phase 2 extension only if they are parallel to the preexisting pervasive anisotropy. The phase 1 faults which form disregarding the anisotropy become inactive during phase 2 extension
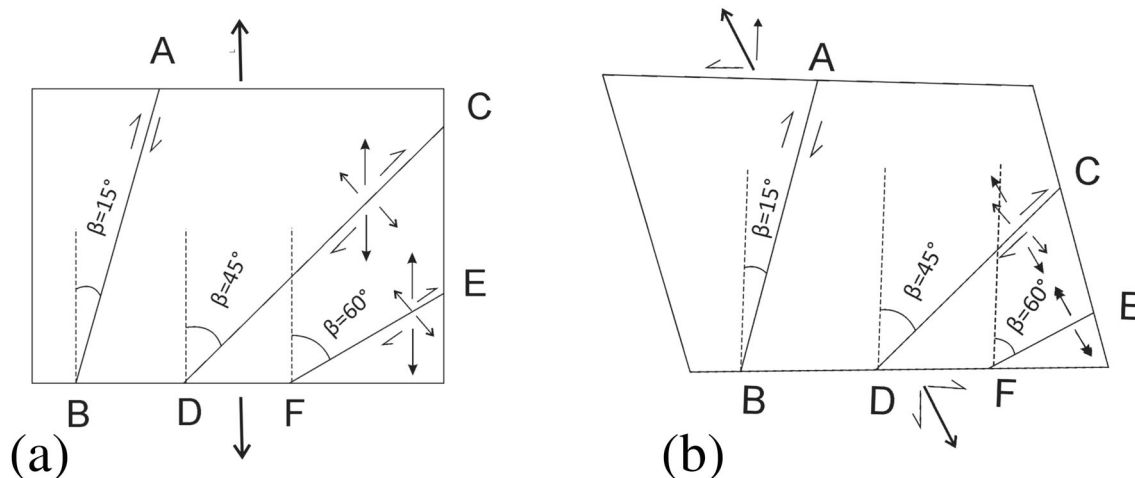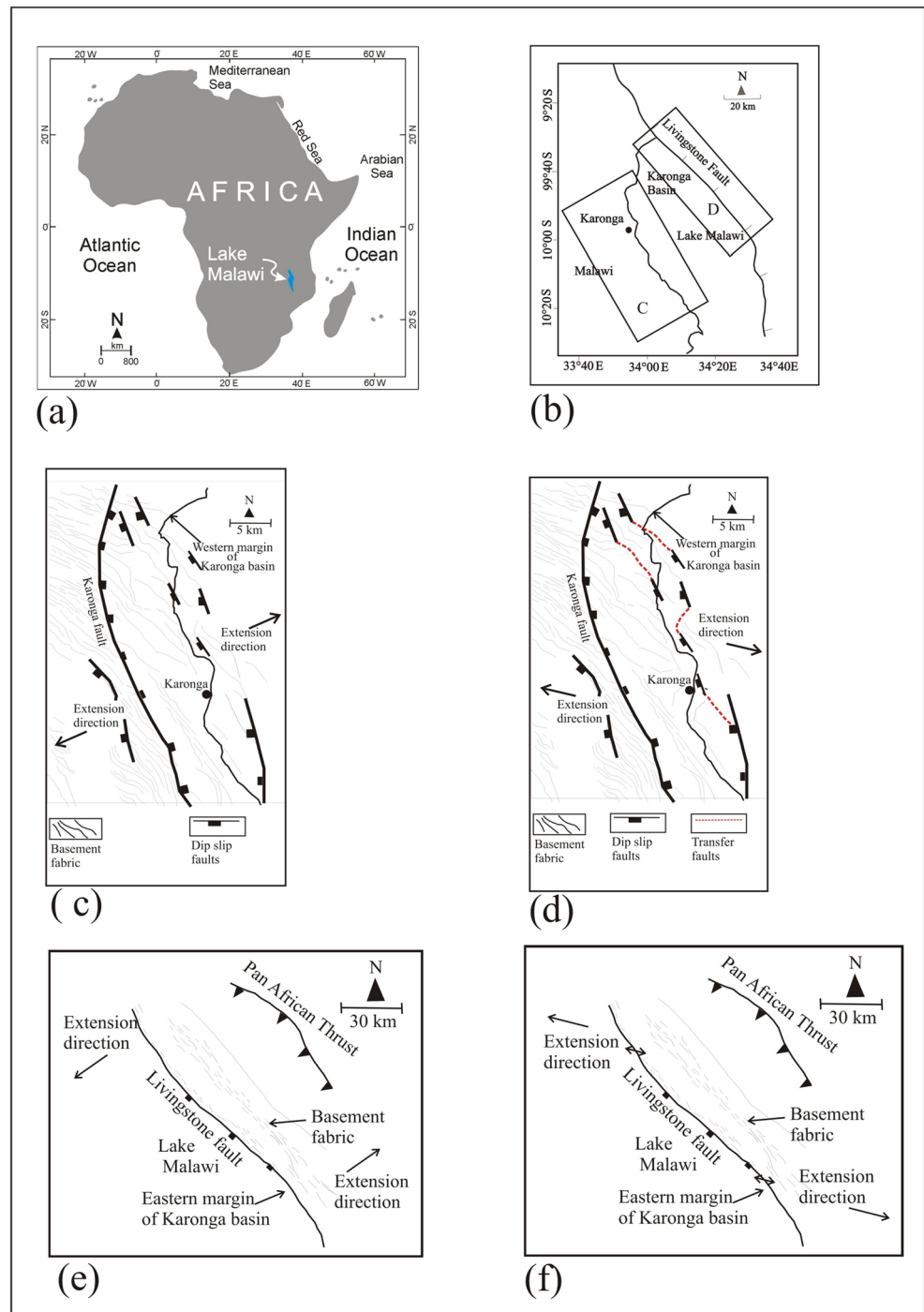

Fig. 16 Schematic diagram showing the growth of differently oriented phase 1 faults during phase 2 deformation. **a** Fault movements during phase 2 orthogonal extension. Less oblique ($\beta = 15°$) phase 1 fault AB grows as dextral strike slip fault. More oblique ($\beta = 45°$) phase 1 fault CD grows as dextral oblique fault. Most oblique ($\beta = 60°$) phase 1 fault EF

grows as dextral oblique fault. **b** Fault movements during phase 2 sinistral oblique extension (at $\alpha = 30°$). Less oblique ($\beta = 15°$) phase 1 fault AB grows as dextral strike slip fault. More oblique ($\beta = 45°$) phase 1 fault CD grows as dextral oblique fault. Most oblique ($\beta = 60°$) phase 1 fault EF grows as dip slip fault

Fig. 17 Natural example of fault patterns from Karonga basin, Malawi Rift, Kenya, Africa which matches with our experimental results. **a** Location showing Malawi rift within Africa. **b** Enlarged sketch of Karonga basin, northern part of Malawi rift (modified from Fig. 2 of Kolawole et al. 2018). **c** Fault patterns in the western part of the Karonga basin, (the area which is marked by square C in **b**) after phase 1 deformation. Here, during Cenozoic rifting, due to initial ENE-WSW orthogonal extension, dip slip faults are formed. These faults cross cut the basement foliations within Precambrian Mugesse shear zone. **d** Fault patterns after two successive phases of deformation in the western margin of the Karonga basin. During 2nd phase of extension in the WNW-ESE direction, transfer faults (oriented SE, ESE, E, and ENE) are formed following direction of the underlying basement shear zone foliations (similar to the results of our experiments 1D). **e** Fault pattern in the Eastern part of the Karonga basin (the area marked by square D in **b**) (modified from Fig. 9a, Ring 1994). During phase 1 ENE-WSW orthogonal extension, the Livingstone Border fault was initiated as a dip slip reactivation of the dominant foliation of the underlying Precambrian shear zone. **f** During late strike slip phase of Cenozoic rifting the Livingstone Border Fault was reactivated as dextral strike slip fault (similar to our experiment 1A)

even if they are oriented more favorably than the pervasive anisotropy and/or the faults following them. Thus, if the preexisting pervasive anisotropy is strong enough to influence the deformation, then it plays a greater role than the discrete phase 1 faults in controlling the final fault pattern, during two successive phases of extensions.

3. During phase 1 extension, the angle between the extension direction and the anisotropy parallel fault has a control on the fault length. A greater angle prefers formation of longer faults.

4. Direction of phase 2 extension plays a role in controlling the development of the faults formed following the more oblique and/or orthogonal anisotropy only. The faults formed following the direction of less oblique anisotropy develop as strike slip faults irrespective of the direction of extension.

Appendix

Scaling of viscous material (pitch)

A model is well scaled to their natural analogues, when the model and its natural prototype remain geometrically, kinematically and dynamically similar (Hubbert 1937; Ramberg 1975). To achieve scaling condition, the model material has to be very weak as experiments are run on real time which is much faster than geological deformations. Geometrical similarity is represented by the model ratio of length (length of the model/length of equivalent natural prototype). For our setup, model ratio of length $(\lambda) = l_m/l_n = 0.2 \times 10^{-5}$ (calculation shown in the Table 4). Kinematic similarity is represented by the model ratio of time (τ). Time ratio is calculated as the ratio of time needed for achieving a certain amount of deformation in the experiment and time needed to achieve the same amount of strain in the corresponding natural situation (Hubbert 1937, p1467). For our setup, model ratio of time $(\tau) = t_m/t_n = 3.8 \times 10^{-11}$ (calculation is shown in the Table 4). Hubbert (1937) suggested that in case of very slowly moving viscous models, the forces due to inertia can be neglected without causing significant error. Consequently, dynamic similarity can be achieved if model ratios of length (l), mass (m), and time (t) are chosen arbitrarily and forces, viz. stress, pressure, shear strength, and viscosity are made to conform to the ratio $\mu = \delta \lambda^3$, where μ, δ, and λ are model ratios of mass,

density and length, respectively (Hubbert 1937, p. 1489). In the present case, we have used viscous models (pitch) under slow strain rate $(\approx 10^{-4}/s)$. Therefore, we have assumed negligible inertial forces following Hubbert's argument. When we compare the model viscosity ratio calculated from the fundamental model ratios $(\zeta = \delta \lambda \tau = 0.34 \times 10^{-16})$ with the actual model ratio of viscosity found in model and its natural analogue (e.g., $\xi = 0.51 \times 10^{-16}$), they are found to be within the same order of magnitude (Table 4). Thus, our models achieve dynamic scaling at least approximately, and the results of our experiments can be reasonably extrapolated to natural situations.

Table 4 Model parameters and scaling ratio

Physical parameters	Pitch	Nature	Model scaling ratio
1. Acceleration due to gravity	$g_m = 9.81$ m/s²	$g_n = 9.81$ m/s²	$g_m/g_n = 1$
2. Length	$l_m = 15$ cm	$l_n = 75$ km	$\lambda = l_m/l_n = 0.2 \times 10^{-5}$
3. Rate of extension	$t_m = 1$ mm/min	$t_n = 1$ cm/year[a]	$\tau = t_m/t_n = 3.8 \times 10^{-11}$
4. Density	$d_m = 1.15$ gm/cm³	$d_n = 2.6$ gm/cm³[b]	$\delta = d_m/d_n = 0.45$
5. Viscosity	$\xi_m = 1.5 \times 10^5$ Pa s[c]	$\xi_n = 2.9 \times 10^{21}$ Pa s[d]	$\xi = 0.51 \times 10^{-16}$

[a] From Cotton and Koyi (2000)

[b] Averaged from the density of granite and that of sedimentary rocks (after Hubbert 1937, Cotton and Koyi 2000)

[c] Viscosity data from Jaeger (1969)

[d] Data from Haskell (cited in Hubbert 1937)

References

Acocella V, Faccenna C, Funiciello R, Rossetti F (1999) Sand-box modelling of basement-controlled transfer zones in extensional domains. Terra Nova-Oxford 11(4):149–156

Agostini A, Bonini M, Corti G, Sani F, Mazzarini F (2011) Fault architecture in the Main Ethiopian Rift and comparison with experimental models: Implicationsfor rift evolution and Nubia-Somalia Kinematics. Earth and Planetary Science Letters 301:479–492. https://doi.org/10.1016/j.epsl.2010.11.024

Ammann N, Liao J, Gerya T, Ball P (2018) Oblique continental rifting and long transform fault formation based on 3D thermomechanical numerical modeling. Tectonophysics 746:106–120. https://doi.org/10.1016/j.tecto.2017.08.015

An L-J, Sammis CG (1996) Development of strike-slip faults: shear experiments in granular materials and clay using a new technique. Journal of Structural Geology 18:1061–1077. https://doi.org/10.1016/0191-8141(96)00012-0

Bellahsen N, Daniel JM (2005) Fault reactivation control on normal fault growth: An experimental study. Journal of Structural Geology 27:769–780. https://doi.org/10.1016/j.jsg.2004.12.003

Bellahsen N, Fournier M, d'Acremont E, Leroy S, Daniel JM (2006) Fault reactivation and rift localization: northeastern Gulf of Aden margin. Tectonics 25(1). https://doi.org/10.1029/2004TC001626

Berenbaum R, Brodie I (1959) Measurement of the tensile strength of brittle materials. British Journal of Applied Physics 10:281–287. https://doi.org/10.1088/0508-3443/10/6/307

Bonini M, Thierry Souriot MB, JPB (1997) Successive orthogonal and oblique extension episodes in a rift zone: laboratory experiments with application to the Ethiopian Rift. Tectonics 16:347–362. https://doi.org/10.1029/96TC03935

Brune S (2016) Rifts and rifted margins: a review of geodynamic processes and natural hazards. Plate Boundaries and Natural Hazards 219:13. https://doi.org/10.1002/9781119054146.ch2

Chakraborty C, Kumar S, Chakraborty G and T (2003) Depositional record of tidal-flat sedimentation in the Permian coal measures of Central India: Barakar formation, Mohpani Coalfield, Satpura Gondwana Basin. Gondwana Research 6:817–827. doi: https://doi.org/10.1016/S1342-937X(05)71027-3

Chattopadhyay A, Chakra M (2013) Influence of pre-existing pervasive fabrics on fault patterns during orthogonal and oblique rifting: An experimental approach. Marine and Petroleum Geology 39:74–91. https://doi.org/10.1016/j.marpetgeo.2012.09.009

Chattopadhyay A, Mandal N (2002) Progressive changes in strain patterns and fold styles in a deforming ductile orogenic wedge: an

experimental study. Journal of Geodynamics 33:353–376. https://doi.org/10.1016/S0264-3707(01)00079-5

Chattopadhyay A, Jain M, Bhattacharjee D (2014) Three-dimensional geometry of thrust surfaces and the origin of sinuous thrust traces in orogenic belts: insights from scaled sandbox experiments. Journal of Structural Geology 69:122–137. https://doi.org/10.1016/J.JSG.2014.09.020

Clifton AE, Schlische RW (2001) Nucleation, growth, and linkage of faults in oblique rift zones: results from experimental clay models and implications for maximum fault size. Geology 29(5):455–458. https://doi.org/10.1130/0091-7613(2001)029<0455:NGALOF>2.0.CO;2

Clifton AE, Schlische RW, Withjack MO, Ackermann RV (2000) Influence of rift obliquity on fault-population systematics: results of experimental clay models. Journal of Structural Geology 22:1491–1509. https://doi.org/10.1016/S0191-8141(00)00043-2

Corti G (2004) Centrifuge modelling of the influence of crustal fabrics on the development of transfer zones: insights into the mechanics of continental rifting architecture. Tectonophysics 384:191–208. https://doi.org/10.1016/J.TECTO.2004.03.014

Corti G, Bonini M, Innocenti F et al (2001) Centrifuge models simulating magma emplacement during oblique rifting. Journal of Geodynamics 31(5):557–576. https://doi.org/10.1016/S0264-3707(01)00032-1

Corti G, van Wijk J, Cloetingh S, Morley CK (2007) Tectonic inheritance and continental rift architecture: numerical and analogue models of the East African Rift system. Tectonics 26:1–13. https://doi.org/10.1029/2006TC002086

Cotton JT, Koyi HA (2000) Modeling of thrust fronts above ductile and frictional detachments: application to structures in the Salt Range and Potwar Plateau, Pakistan. Geol. Soc. Am. Bull 112(3):351–363

Daly MC, Chorowicz J, Fairhead JD (1989) Rift basin evolution in Africa: the influence of reactivated steep basement shear zones. Geological Society, London, Special Publications 44(1):309–334. https://doi.org/10.1144/GSL.SP.1989.044.01.17

Dauteuil O, Brun J-P (1993) Oblique rifting in a slow-spreading ridge. Nature 361:145–148. https://doi.org/10.1038/361145a0

Davy P, Cobbold PR (1988) Indentation tectonics in nature and experiment. 1. Experiments scaled for gravity. Bull. Geol. Inst. Univ. Uppsala 14:129–141

Deng C, Gawthorpe RL, Fossen H, Finch E (2018) How does the orientation of a preexisting basement weakness influence fault development during renewed rifting? Insights from three-dimensional discrete element modeling. Tectonics 37(7):2221–2242. https://doi.org/10.1029/2017TC004776

Dubois A, Odonne F, Massonnat G et al (2002) Analogue modelling of fault reactivation: tectonic inversion and oblique remobilisation of grabens. Journal of Structural Geology 24:1741–1752. https://doi.org/10.1016/S0191-8141(01)00129-8

Fournier M, Petit C (2007) Oblique rifting at oceanic ridges: relationship between spreading and stretching directions from earthquake focal mechanisms. Journal of Structural Geology 29(2):201–208. https://doi.org/10.1016/j.jsg.2006.07.017

Ghosh N, Chakra M, Chattopadhyay A (2014) An experimental approach to strain pattern and folding in unconfined and/or partitioned transpressional deformation. International Journal of Earth Sciences 103:349–365. https://doi.org/10.1007/s00531-013-0951-z

Ghosh N, Hatui K, Chattopadhyay A (2019) Propagation and coalescence of en-echelon cracks under a far-field tensile stress regime: An experimental study. Journal of Earth System Science 128:1–16. https://doi.org/10.1007/s12040-018-1056-7

Henza AA, Withjack MO, Schlische RW (2011) How do the properties of a pre-existing normal-fault population influence fault development during a subsequent phase of extension? Journal of Structural Geology 33:1312–1324. https://doi.org/10.1016/j.jsg.2011.06.010

Hetzel R, Strecker MR (1994) Late Mozambique Belt structures in western Kenya and their influence on the evolution of the Cenozoic Kenya Rift. Journal of Structural Geology 16:189–201. https://doi.org/10.1016/0191-8141(94)90104-X

Hubbert MK (1937) Theory of scale models as applied to the study of geologic structures. Bulletin Geological Society of America 48(10):1459–1520

Hus R, Acocella V, Funiciello R, De Batist M (2005) Sandbox models of relay ramp structure and evolution. Journal of Structural Geology 27(3):459–473. https://doi.org/10.1016/j.jsg.2004.09.004

Jaeger JC (1969) Elasticity, fracture and flow with engineering and geological applications. Methuen & Co. Ltd, and Science Paperbacks, John Wiley & Sons, Inc., New York

Keep M, McClay KR (1997) Analogue modelling of multiphase rift systems. Tectonophysics 273:239–270. https://doi.org/10.1016/S0040-1951(96)00272-7

Kolawole F, Atekwana EA, Laó-Dávila DA, Abdelsalam MG, Chindandali PR, Salima J, Kalindekafe L (2018) Active deformation of Malawi rift's north basin hinge zone modulated by reactivation of preexisting Precambrian shear zone fabric. Tectonics 37(3):683–704. https://doi.org/10.1002/2017TC004628

Mandal N (1995) Mode of development of sigmoidal en echelon fractures. Proc. Indian Acad. of Sci-Earth and Planet. Sci. 104(3):453–464. https://doi.org/10.1007/BF02843409

Mauduit T, Dauteuil O (1996) Small-scale models of oceanic transform zones. Journal of Geophysical Research - Solid Earth 101:20195–20209. https://doi.org/10.1029/96JB01509

McClay KR, White MJ (1995) Analogue modelling of orthogonal and oblique rifting. Marine and Petroleum Geology 12:137–151. https://doi.org/10.1016/0264-8172(95)92835-K

McConnell RB (1972) Geological development of the rift system of eastern Africa. GSA Bulletin 83:2549–2572. https://doi.org/10.1130/0016-7606(1972)83[2549:GDOTRS]2.0.CO;2

Morley CK (1999) How successful are analogue models in addressing the influence of pre-existing fabrics on rift structure? Journal of Structural Geology 21:1267–1274. https://doi.org/10.1016/S0191-8141(99)00075-9

Morley CK, Haranya C, Phoosongsee W et al (2004) Activation of rift oblique and rift parallel pre-existing fabrics during extension and their effect on deformation style: examples from the rifts of Thailand. Journal of Structural Geology 26:1803–1829. https://doi.org/10.1016/j.jsg.2004.02.014

Nott JA (2009) Tensile strength and failure criterion of analog lithophysal rock. https://digitalscholarship.unlv.edu/thesesdissertations/116

Peace A, Mccaffrey K, Imber J et al (2017) The role of pre-existing structures during rifting, continental breakup and transform system development, offshoreWest Greenland. Basin Research 30:373–394. https://doi.org/10.1111/bre.12257

Peace A, Dempsey E, Schiffer C et al (2018) Evidence for basement reactivation during the opening of the Labrador Sea from the Makkovik Province, Labrador, Canada: insights from field data and numerical models. Geosciences 8(8):308. https://doi.org/10.3390/geosciences8080308

Philippon M, Willingshofer E, Sokoutis D, Corti G, Sani F, Bonini M, Cloetingh S (2015) Slip re-orientation in oblique rifts. Geology 43(2):147–150. https://doi.org/10.1130/G36208.1

Ramberg H (1975) Particle paths, displacements and progressive strain applicable to rocks. Tectonophysics 28:1–37. https://doi.org/10.1016/0040-1951(75)90058-X

Ring U (1994) The influence of preexisting structure on the evolution of the Cenozoic Malawi rift (East African rift system). Tectonics 13:313–326. https://doi.org/10.1029/93TC03188

Schön JH (2011) Rocks—their classification and general properties. In Handbook of Petroleum Exploration and Production. Elsevier 8:1–16. https://doi.org/10.1016/S1567-8032(11)08001-3

Serra S, Nelson RA (1988) Clay modeling of rift asymmetry and associated structures. Tectonophysics 153:307–312. https://doi.org/10.1016/0040-1951(88)90023-6

Teyssier C, Tikoff B, Markley M (1995) Oblique plate motion and continental tectonics. Geology 23(5):447–450

Theunissen K, Klerkx J, Melnikov A, Mruma AH (1996) Mechanisms of inheritance of rift faulting in the western branch of the East African Rift, Tanzania. Tectonics 15:776–790. https://doi.org/10.1029/95TC03685

Thomas AL, Pollard DD (1993) The geometry of echelon fractures in rock: implications from laboratory and numerical experiments. Journal of Structural Geology 15:323–334. https://doi.org/10.1016/0191-8141(93)90129-X

Tron V, Brun JP (1991) Experiments on oblique rifting in brittle-ductile systems. Tectonophysics 188:71–84. https://doi.org/10.1016/0040-1951(91)90315-J

Vekinis G, Ashby MF, Beaumont PWR (1993) Plaster of Paris as a model material for brittle porous solids. Journal of Materials Science 28(12):3221–3227

Wilson RW, Holdsworth RE, Wild LE et al (2010) Basement-influenced rifting and basin development: a reappraisal of post-Caledonian faulting patterns from the North Coast Transfer Zone, Scotland. Geol Soc London, Spec Publ 335:795–LP-826. https://doi.org/10.1144/SP335.32

Withjack MO, Jamison WR (1986) Deformation produced by oblique rifting. Tectonophysics 126:99–124. https://doi.org/10.1016/0040-1951(86)90222-2

Zwaan F, Schreurs G (2017) How oblique extension and structural inheritance influence rift segment interaction: insights from 4D analog models. Interpretation 5:SD119–SD138. https://doi.org/10.1190/INT-2016-0063.1

Zwaan F, Schreurs G, Buiter S (2019) 4D X-ray CT data and surface view videos of a systematic comparison of experimental set-ups for modelling extensional tectonics. https://doi.org/10.5880/fidgeo.2019.018

Publisher's note Springer Nature remains neutral with regard to jurisdictional claims in published maps and institutional affiliations.